A&A, 709, A275 (2026)
https://doi.org/10.1051/0004-6361/202557865
© The Authors 2026

Astronomy & Astrophysics

The average X-ray spectrum of the volume-complete M-, F-, G-, and K-type star sample within 10 pc of the Sun

Xueying Zheng[1,⋆], Gabriele Ponti[2,1,3], Nicola Locatelli[2], Beate Stelzer[4], Enza Magaudda[4], Konrad Dennerl[1], Michael J. Freyberg[1], Jeremy Sanders[1], Marilena Caramazza[4], Manami Sasaki[5], Andrea Merloni[1], Jan Robrade[6], Teng Liu[1,7,8], He-shou Zhang[2], Martin G. F. Mayer[5], Yi Zhang[1,10], Michael C. H. Yeung[1], and Werner Becker[1,9]

[1] Max-Planck-Institut für extraterrestrische Physik, Gießenbachstraße 1, 85748 Garching bei München, Germany
[2] INAF – Osservatorio Astronomico di Brera, Via E. Bianchi 46, 23807 Merate (LC), Italy
[3] Como Lake centre for AstroPhysics (CLAP), DiSAT, Università dell'Insubria, via Valleggio 11, 22100 Como, Italy
[4] Institut für Astronomie und Astrophysik, Eberhard Karls Universität Tübingen, Sand 1, 72076 Tübingen, Germany
[5] Dr. Karl Remeis Observatory, Erlangen Centre for Astroparticle Physics, Friedrich-Alexander-Universität Erlangen-Nürnberg Sternwartstraße 7, 96049 Bamberg, Germany
[6] Hamburger Sternwarte, Gojenbergsweg 112, 21029 Hamburg, Germany
[7] Department of Astronomy, University of Science and Technology of China, Hefei 230026, China
[8] School of Astronomy and Space Science, University of Science and Technology of China, Hefei 230026, China
[9] Max-Planck-Institut für Radioastronomie, Auf dem Hügel 69, 53121 Bonn, Germany
[10] Max-Planck-Institut für Astrophysik, Karl-Schwarzschild-Straße 1, 85748 Garching, Germany

Received 28 October 2025 / Accepted 23 February 2026

ABSTRACT

Context. The F-, G-, K-, and M-type stars are the most abundant stellar population in the Milky Way and are expected to contribute to its diffuse X-ray emission. Yet their intrinsic average X-ray spectrum remains poorly constrained due to their faint X-ray luminosities, leaving their collective role in the X-ray background of the Milky Way uncertain.
Aims. We aim to derive a distance-normalised average X-ray spectrum for nearby M dwarfs and F, G, and K stars and to characterise their ensemble spectral properties.
Methods. We analysed the volume-complete sample of M dwarfs (M0–M6) and F, G, and K stars within 10 pc of the Sun using data from the *eROSITA* all-sky survey aboard the Spectrum-Roentgen-Gamma (SRG) mission (eRASS:4). Individual spectra were normalised by exposure and distance and then stacked to produce representative averages. From these spectra, we derived characteristic X-ray luminosities, which are helpful for estimating the contribution of late-type stars to the soft, diffuse X-ray emission of the Galaxy.
Results. The distance-normalised emission measures yield an average X-ray luminosity of $(2.6 \pm 0.1) \times 10^{27}$ erg/s for M-type stars, and $(15 \pm 3) \times 10^{27}$ erg/s for F-, G-, and K-type stars in 0.2–2.0 keV. The 10-pc average spectra could be well described by a sum of three and two thermal models. The fitted temperatures and abundances remain consistent across M-star sub-groups, while early-M stars are, surprisingly, less luminous on average than mid-to-late-M types. These results offer new insights into the collective X-ray properties of nearby stars in the volume-complete context, and provide motivation to further explore the link with the unresolved soft X-ray background of the Galaxy.

Key words. stars: coronae – stars: late-type – stars: low-mass – X-rays: stars

1. Introduction

Late-type main-sequence stars, such as F-, G-, K-, and M-type stars, are the most numerous stellar type in the Milky Way. M dwarfs alone account for about 70% of the entire stellar population, yet they contribute only about 35% of the total stellar mass. FGK-type stars, though less common (∼23%), provide a comparable fraction of stellar mass (∼35%) (Reid & Gizis 1997; Bochanski et al. 2010; Golovin et al. 2023; Kirkpatrick et al. 2024). Their X-ray emission arises from magnetically heated coronae, where plasma is confined and energised by magnetic fields generated through convection and rotation (Parker 1993; Güdel 2004). Understanding this emission is crucial, as it serves as a proxy for their dynamo and shapes the environments of surrounding planets. Individually, these stars appear as faint X-ray sources even at close distances, but their sheer numbers suggest that they contribute significantly to the soft X-ray background, including the local hot bubble and Galactic halo (Yeung et al. 2024; Ponti et al., in prep.).

A systematic census of the X-ray emission from nearby late-type stars was first carried out with the *ROSAT* All-Sky Survey, led by Schmitt & Liefke (2004) who compiled the ROSAT/NEXXUS catalogue of all stars in the solar neighbourhood. Deeper observations involving *XMM-Newton* and *Chandra*, combined with *ROSAT*, have since enabled detailed spectral investigations of individual stars. Multi-temperature collisionally ionized thermal model has provided good fits to these stellar coronae, such as in AD Leonis, EV Lac, and EQ Pegasi (Raymond & Smith 1977; Mewe 1991; Robrade & Schmitt 2005).

More recent efforts have been directed towards fully characterising the X-ray properties of volume-limited samples through

⋆ Corresponding author: zhengxy@mpe.mpg.de

Open Access article, published by EDP Sciences, under the terms of the Creative Commons Attribution License (https://creativecommons.org/licenses/by/4.0), which permits unrestricted use, distribution, and reproduction in any medium, provided the original work is properly cited.
This article is published in open access under the Subscribe to Open model. Open access funding provided by Max Planck Society.

systematic surveys with the help of *Gaia*. Based on the *Gaia* 10-pc catalogue (Reylé et al. 2021), Caramazza et al. (2023) conducted the census of X-ray observations of M dwarfs within the closest 10 pc using *ROSAT*, *XMM-Newton*, and *eROSITA*, probing the faintest levels of coronal emission. Zhu & Preibisch (2025) and Locatelli et al. (2025) also combined the archival X-ray data to study the distribution of luminosity of nearby stars of F to M type in different volumes. Together, these studies provide important constraints on the prevalence and distribution of stellar X-ray activity, with an emphasis on individual luminosity measurements and their relation to other stellar properties.

In this work, we built on these efforts by deriving a distance-normalised stacked X-ray spectrum from the complete, volume-limited sample of nearby late-type stars using data from the four sky surveys of *eROSITA* (eRASS:4; see Section 3). Our stellar sample is based on the *Gaia* 10-pc catalogue (Reylé et al. 2021), with the M-dwarf sub-sample (M0–M4) and their coordinates provided by Caramazza et al. (2023), and the complementary M4–M6 and FGK-dwarf lists supplied by Stelzer (priv. comm.). We extracted spectra from the merged *eROSITA* eRASS:4 event files and stacked them to yield an emissivity-weighted average luminosity for M stars and FGK stars separately.

The paper is structured as follows. The data-selection procedure is described in Section 2; Section 3 presents the data processing; Section 4 explains the stacking approach; Section 6 introduces model fitting and spectral analysis for the averaged spectrum of M0–M6 stars within 10 pc; Section 7 discusses the spectral analysis of FGK-type stars within 10 pc; and finally, Section 9 summarises the results.

2. Sample selection

As mentioned above, we used the volume-complete *Gaia*-based catalogue of stars within 10 pc of the Sun (Reylé et al. 2021) as the master sample. From this, we adopted the F, G, K, and M0–M6 spectral type (SpT) sub-sample defined by Stelzer et al.(in prep.), which, following Caramazza et al. (2023), assigned a SpT based on *Gaia* eDR3 $G_{BP} - G_{RP}$ colours using the conversion table compiled by E. Mamajek[1]. We then restricted the selection to stars located in the western Galactic hemisphere ($l \geq 180°$, hereafter WGH), which is accessible to the SRG/eROSITA_DE collaboration.

2.1. Sample overview

Table 1 summarises the number of stars for the sample selection. In total, the 10-pc *Gaia* catalogue contains 225 M0–M6-type stars and 57 FGK-type stars, of which 109 are M stars, and 32 FGK stars are located in the WGH.

We removed four M stars (IDs 35, 45, 51, and 208; index from Table H.1) and two FGK stars (ID 0 and ID 43; index from Table H.2) due to close proximity to other SpT X-ray sources ('crowded field' sources in Table 1). In addition, two M stars (ID 137, 157) were excluded from the final sample due to optical loading. We mark pairs of the same SpT stars separated by less than 5″ as 'close pairs' and extracted a single spectrum from a common region encompassing both sources to avoid duplication (see Appendix C for details on the spectral extraction). Eventually, 103 M stars remained after excluding the two stars affected by optical loading (see also Appendix A), constituting the final M-dwarf sample used in this work. We did not exclude FGK stars affected by optical loading (22 of the 32), as excluding them would have severely reduced the completeness of the sample. The final FGK sample to be stacked still comprises 30 stars. In Sect. 2.2 and Appendix A, we compare these 22 optically bright FGK stars' X-ray fluxes with those of the nine optically faint FGK stars and discuss how the impact of optical loading depends on optical brightness.

Table 1. Sample selection in this work based on *Gaia* 10-pc M-type and F-, G-, and K-type stars (Stelzer, priv. comm.).

Selection/Flag	M stars (N)	FGK stars (N)
Gaia 10 pc	225	62
Western Hemisphere	109	32
Flag A: crowded field	4	2
Flag B: optical loading	2 (excluded)	22 (retained)
Flag C: close pair	10	3
Remaining (used in this work)	103 (Flag AlB = 0)	30 (Flag A = 0)

In Figure 1, we present the eRASS1-detected (Merloni et al. 2024) M-type and F-, G-, and K-type stars that are used in our sample, showing X-ray luminosity versus *Gaia* colour (left panel) and total observed counts versus distance for all stars, regardless of whether they were detected in eRASS1 (right panel). Five FGK stars, α Cen A, α Cen B, Procyon A, and HD 156384 A and B, are not shown in Figure 1 as they lack *Gaia* measurements due to brightness saturation (Reylé et al. (2021)). The sample used in this paper has a wider SpT range for M stars (M0–M6) compared to that of Caramazza et al. (2023), which measured the X-ray luminosity of all the detected M0–M4 stars within 10 pc in both the eastern and western hemispheres. According to the luminosity distribution, M stars (M0–M4) in the eastern Galactic hemisphere (EGH) appear to host more high-luminosity sources than the western Galactic hemisphere (WGH). Several of the most luminous M stars, such as AU Mic, AT Mic A, and GJ 867 A and B, are in fact located in the EGH. On average, M stars in the EGH are about 4.7 times more luminous than those in the WGH. For FGK stars (Stelzer, in prep.), the average luminosity in the WGH is slightly higher than in the EGH, i.e. by a factor of about 1.3. Therefore, if one estimates the average luminosity from the EGH, the result can be larger than the one we obtain in this work as our data are limited to the WGH. In Appendix H, we provide the identifiers, coordinates, distances, spectral types, the eRASS1 detection flag (Merloni et al. 2024), and the selection flag of the individual stars used in this work.

2.2. Optical loading

In X-ray astronomy, optical loading refers to the interference caused by non-X-ray radiation, such as optical or ultraviolet light, on X-ray detectors (Lumb 2000). While these detectors are primarily designed to detect X-rays, they can also exhibit sensitivity to other types of radiation, which can introduce noise and false signals, particularly in the soft X-ray regime (Ramstedt et al. 2012; Ishikawa et al. 2019). Optical loading can artificially enhance the soft X-ray signal and potentially shift the measured energy of events across the entire spectrum.

[1] https://www.pas.rochester.edu/~emamajek/EEM_dwarf_UBVIJHK_colors_Teff.txt

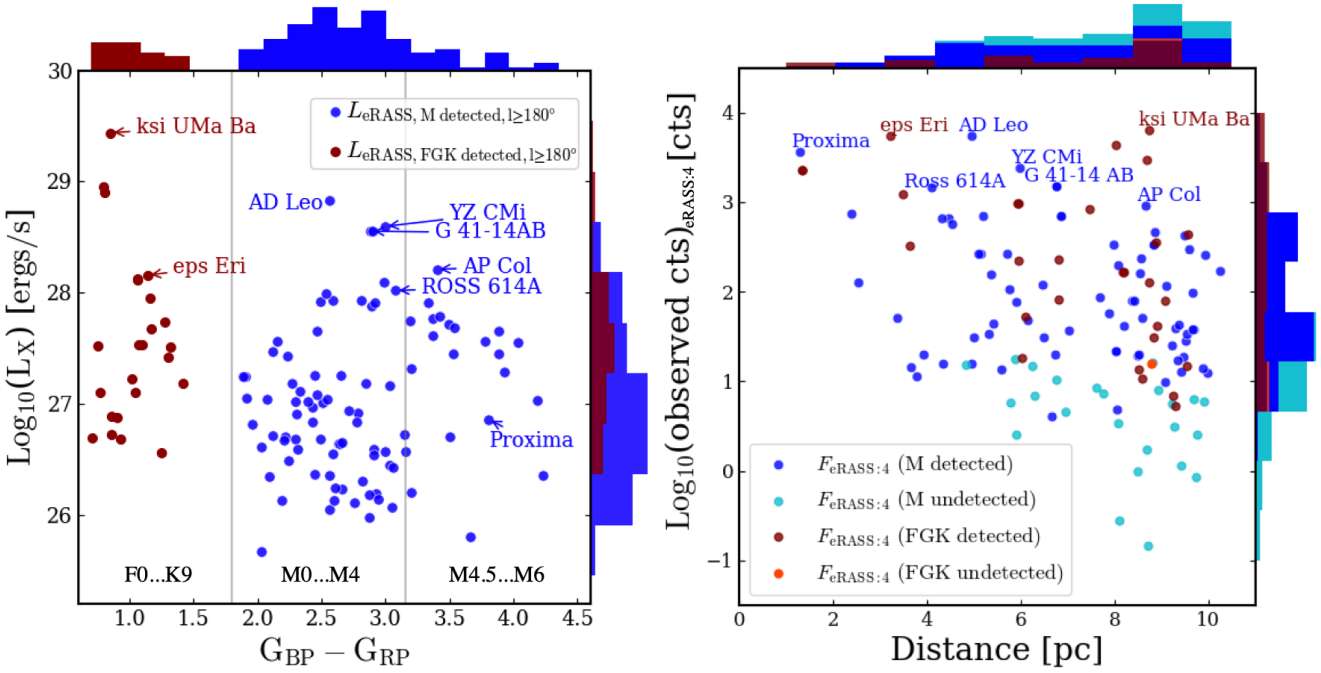

Fig. 1. Left: X-ray luminosity (0.1–2.4 keV) versus *Gaia* G_{BP}-G_{RP} colour for the eRASS1-detected M- and FGK-type stars (Merloni et al. 2024) in the western Galactic hemisphere of the 10-pc *Gaia* sample. Filled blue circles: eRASS1-detected M dwarfs ($l \geq 180°$); filled red circles: eRASS1-detected FGK stars ($l \geq 180°$). Notable sources are labeled. Right: eRASS:4 total observed counts in 0.2–2.0 keV versus the distance from the Sun for the 10-pc *Gaia* sample in the western Galactic hemisphere, with detections and non-detections for M dwarfs (blue, cyan) and FGK stars (brown, coral).

To mitigate this effect, we adopted the FLAG_OPT indicator from the eRASS1 catalogue (Merloni et al. 2024), which flags sources potentially affected by optical loading. A source is assigned FLAG_OPT = 1 if it is located within 15″ of a bright optical star (including the source itself) that meets any of the following brightness thresholds: B, V, or G < 4.5 mag, or J < 3 mag. However, the optical-loading threshold also depends on the survey depth; while G<4.5 mag was used for eRASS1, a threshold of G<5.0 mag is more appropriate for eRASS:4 (J. Robrade, priv. comm.).

In Figure 2, we can see no M stars in our sample suffering from optical loading (G < 5), in contrast to more than half of the FGK stars. This result was expected, as the FGK stars are stronger optical emitters than M-dwarf stars. However, as noted earlier, two M-dwarf stars were excluded due to optical loading: GJ 166 C based on its FLAG_OPT indicator; and GJ 442 B, which is part of a visual binary with a separation of 22″ from the bright G-type primary star (GJ 442 A) affected by optical loading.

A detailed explanation of this effect, based on current knowledge of SRG/eROSITA and supported by spectral analysis, is provided in Appendix A. Figure A.2 compares M dwarfs and FGK dwarfs with different G-band magnitudes, showing that M stars' spectra are consistent and confirming that optical loading has a negligible impact on the M-dwarf sample. In contrast, for FGK stars, a similar test reveals differences on both luminosity and spectral shape, which could originate from optical-loading effects (and the intrinsic luminosity scatter for this limited sample). In Figures A.1a–A.1d, we show three selected FGK stars (G < 5) as examples to examine the possible impact of optical loading by comparing photon-event pattern selections (single, s) with the combined double+triple+quadruple selection (dtq). To obtain a representative average luminosity, we retained all

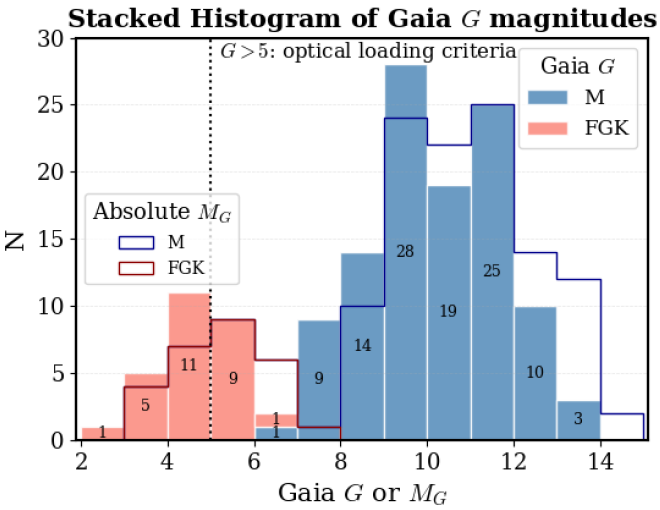

Fig. 2. Histogram of *Gaia* G apparent (G, filled bars) and absolute (M_G, outlined bars) magnitudes of the M-type (blue) and FGK-type (red) stars used in this study. The G mag and parallax were taken from Reylé et al. (2021). Five stars with *Gaia*- saturated magnitudes are not shown here. The vertical dashed line marks the optical loading threshold adopted in this work (G > 5; Robrade, priv. comm.).

FGK stars but truncated the soft-energy range (<0.35 keV) in this study.

3. Data processing

The *eROSITA* survey detected most of the late-type stars in the 10-pc *Gaia* sample (about 75% in eRASS1; Merloni et al. 2024; and over 90% in eRASS:4, in prep.) and scanned all

its stars four times over two years, from 2019 December 11 to 2021 December 19. The eROSITA/eRASS:4 data were processed using the standard *eROSITA* Science Analysis Software System (eSASS), version `eSASSusers_240410`, developed by the German eROSITA consortium (Brunner et al. 2022). For this study, we used event files from five telescope modules (`TMs`) with on-chip filters (`TM1,2,3,4,6`), the combination of which is referred to as `TM8`. Two modules (`TM5` and `TM7`) lack on-chip optical filters and suffer from light leaks (Predehl et al. 2021), so they were excluded from this study. Using the eSASS task `evtool`, event files from all four eRASS surveys were combined to create a single event set. All the spectra were collected with all valid patterns (`PAT15`) when not explicitly mentioned.

4. Method: Spectral stacking

To stack the spectra of stars in the sample, the extraction region for each source was first adjusted to account for proper motion, aligning all positions to a standard reference epoch, 2020 December 15 (Merloni et al. 2012). A single spectrum was generated for each star by merging data from all four eRASS observations (see Appendix C for further details on the extraction procedure). In cases where two stars fell too close together (within 25″), only one combined spectrum was extracted, and both the source and background fluxes were scaled by a factor of two. Each resulting spectrum was then normalized to a reference distance of 10 pc using a scaling factor of $(d_i/10\ \mathrm{pc})^2$, where d_i is the distance to the star. The background subtraction was performed locally for each source.

Below, we present the full equation used to compute the average rates along with the associated uncertainty:

$$C_{\mathrm{net,total}} = \sum_{i=1}^{N}\left[\left(C_{\mathrm{src},i} - C_{\mathrm{bkg},i}\cdot S_i\right)\left(\frac{d_i}{10\ \mathrm{pc}}\right)^2\right], \tag{1}$$

$$< R > = \frac{C_{\mathrm{net,total}}}{\sum_{i=1}^{N} T_i}, \tag{2}$$

$$< E_R > = \frac{\sqrt{C_{\mathrm{net,total}}}}{\sum_{i=1}^{N} T_i} = \sqrt{\frac{< R >}{\sum_{i=1}^{N} T_i.}} \tag{3}$$

$C_{\mathrm{src},i}$ and $C_{\mathrm{bkg},i}$ denote the counts of source region and background from the i-th star, $< R >$ is the averaged count rate of the i-th star, d_i is its distance in pc, T_i is the exposure time processed by `srctool`, N is the total number of stars in the sample, and S_i is the scaling factor between a source region and background region. The uncertainties in the stacked spectrum, $< E_R >$, reflect the combined Gaussian errors propagated from the individual source spectra. Depending on the definition of stacking, there are multiple ways to combine spectra. The approach described in Eq. (2), which we refer to as the 'averaging count' (AC) method, is what we mainly used in this work. Since individual rate varies, the average rate can be more strongly influenced by stars with longer exposures. While approximately 90% of the stars have similar exposure times (processed by `srctool`) within one standard deviation, a few sources located near the ecliptic pole have significantly longer exposures and therefore might receive much higher weights. To ensure that these high-weight sources do not bias the average spectrum, we also performed additional stacking without them. A comparison of the results with and without these stars is presented in Appendix B.

Alternatively, we could apply the 'averaging rate' (AR) method for spectral stacking (Eqs. (4)–(6)). Instead of summing

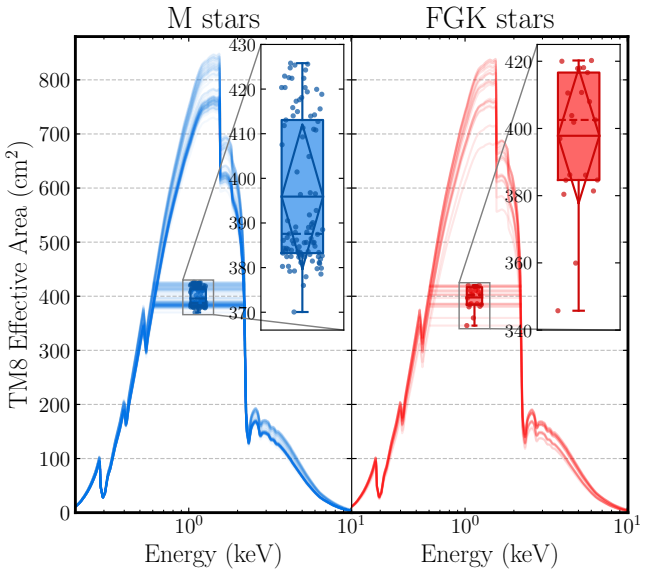

Fig. 3. Comparison of effective area of `TM8`. The box plot represents the statistical distribution of the mean effective area over the 0.2–2.0 keV range. The solid horizontal lines within each box indicate the average value, while the dashed horizontal line (in the zoomed-in plot) represents the median. The sample includes all 103 M stars and 30 FGK stars used in this study.

total counts and dividing by total exposure time, this approach computes the average of the count rates across individual sources for each energy channel. Specifically, for each star, the count rate is distance-corrected and then averaged over all sources. The method is mathematically expressed as

$$< R > = \frac{\sum_{i=1}^{N}(C_{\mathrm{src},i} - C_{\mathrm{bkg},i}\cdot S_i)/T_i \cdot \left(\frac{d_i}{10\ pc}\right)^2}{N} \tag{4}$$

$$< C > = < R > \cdot \sum_{i=1}^{N} T_i \tag{5}$$

$$< E_R > = \frac{\sqrt{\sum_{i=1}^{N}(C_{\mathrm{src},i} + C_{\mathrm{bkg},i}\cdot S_i^2)\cdot(1/T_i\cdot\left(\frac{d_i}{10\ pc}\right)^2)^2}}{N,} \tag{6}$$

where the denotation is the same as Eqs. (1)–(3). This approach normalises counts by exposure before averaging, which ensures each source contributes according to its count rate. However, because standard error propagation assumes statistical independence, it can lead to overestimated uncertainties when stacking spectra with correlated measurements or shared systematics. To mitigate this, we adopted a Gaussian noise assumption, which provides a lower bound on the uncertainties, acknowledging that this likely underestimates the actual statistical error. In Appendix B, we compare the resulting fits and luminosities from this method with those obtained using the AC approach. The differences between them are treated as a source of systematic uncertainty in the final luminosity estimates.

In Appendix B, we compare the best-fit parameters and luminosities obtained from the AC and AR methods, as well as when excluding highly exposed sources, confirming that the stacking procedure does not significantly affect the overall spectral shape.

Given that the effective area of the detector varies with vignetting and masking in the source region, an averaged effective area was computed in each PI channel. While this method

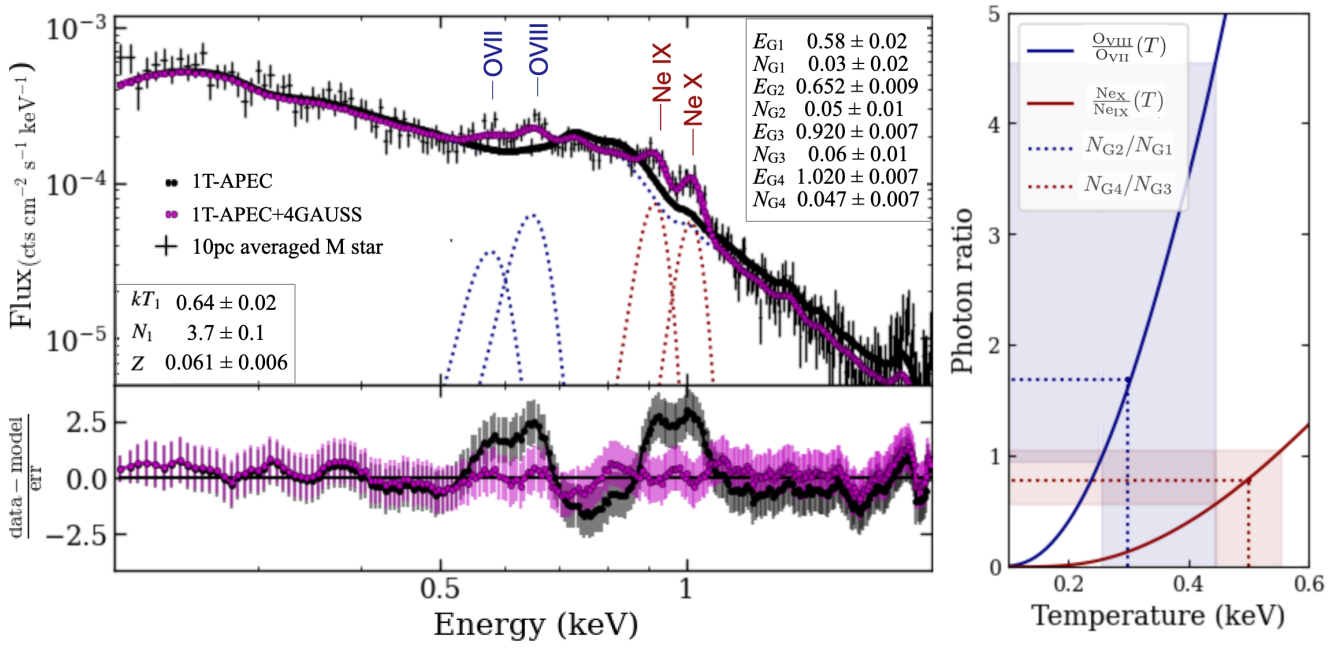

Fig. 4. Left panel: averaged 10-pc M-dwarf spectrum with different models. All the models are labelled in the legend, where names follow the XSPEC convention, and the letter G stands for the Gaussian components used to fit single emission lines (dotted lines). Right panel: temperature versus line ratio assuming a single thermal component. The dark red and navy lines show the expected O VIII/O VII and Ne X/Ne IX ratios from AtomDB. Vertical dashed and dotted lines mark ratios derived from Gaussian normalisations in Table 2.

is not theoretically optimal, it provides a practical and reproducible approach. Figure 3 presents a statistical comparison of the effective area of TM8 for the sample of 103 M stars and 30 FGK stars. The box plot displays the distribution of the mean effective area. In each box, the solid horizontal line represents the mean value of the sample, while the dashed line indicates the median value. Variations in the effective area amongst sources were mainly caused by masking nearby point sources, with the maximum discrepancies reaching approximately 10% for both samples, as illustrated in the box plot.

5. Analysis: Spectral fitting

The spectral fitting was performed using the pyXspec software (Arnaud 1996). The fitting process assumed elemental abundances from Asplund et al. (2009) and photoelectric absorption cross-sections from Verner et al. (1996). χ^2 minimisation was used for the fitting.

Our analysis assumed that the emitting plasma is in collisional ionisation equilibrium (CIE) (Raymond & Smith 1977; Güdel 2004). The analysis begins with a single-temperature, collisionally ionised plasma model, i.e. Astrophysical Plasma Emission Code model (APEC and VAPEC; Smith et al. 2001), which describes a collisionally ionised plasma in stellar coronae of thermal equilibrium. It then progresses towards more complex models, including multi-temperature (2T-APEC and 3T-APEC) (Smith et al. 2001) and variable abundance models (1T-VAPEC, 2T-VAPEC, and 3T-VAPEC). The elemental abundances are tied across all thermal components.

We denote the overall metallicity by Z and the abundance of a specific element by A_X. The metal abundance (A_X) is defined as $A_{\rm element} = \frac{(n_Z/n_H)_{\rm plasma}}{(n_Z/n_H)_\odot}$. With the VAPEC model, we allowed O, Ne, Si, and Fe to vary independently; all other elements (He, C, N, Mg, Al, S, Ar, Ca, Ni) were tied together and allowed to vary as a single free parameter. Alpha elements such as oxygen, neon, and silicon were primarily considered (Bensby et al. 2014; Jofré et al. 2015; Montes et al. 2018). We verified that we could not obtain improvement in the fit by untying any of the abundances of the other elements. More parameter initializations are listed in Appendix D.

To assess the relative quality of spectral fits, we employed the Fisher test (F-test), the Bayesian information criterion (BIC; Schwarz 1978), and the Akaike information criterion (AIC; Akaike 1974). The F-test evaluates whether the addition of extra parameters significantly improves the fit, assuming nested models and Gaussian errors. The AIC and BIC are both information-theoretic criteria that balance model goodness of fit against complexity, with the BIC applying a penalty for the complex models. In our case, we adopted AIC=$2k + \chi^2_{\rm stat}$ and BIC=$k\ \ln(N) + \chi^2_{\rm stat}$, where k is the number of free parameters and N is the number of data channels.

6. Results: M-dwarf sample

In this section, we describe how we fitted the average X-ray spectrum of M dwarfs. Unless stated otherwise, the M-star spectra were fitted within the energy range of 0.2–2.0 keV, where the signal-to-noise ratio (S/N) of the stacked spectra, which is scaled to 10 pc, exceeds one.

The results of the fitting procedure for the sequence of models are summarized in Table 2, while the corresponding multi-temperature spectral fits are presented in Figure 5. The uncertainties correspond to 90% confidence intervals for a single parameter assuming chi-squared statistics. The bootstrap uncertainties (90% CI) are reported as the second term in the brackets of the corresponding parameter. The F tests between models are provided in Table 3.

Table 2. Model parameters and values for M-dwarf averaged spectrum.

Param.	APEC	VAPEC	2T-APEC	2T-VAPEC	3T-APEC	3T-VAPEC		APEC +GAUSS
kT_1	0.66 ± 0.02	0.46 ± 0.02	$0.27\ (\pm 0.01, \pm 0.01)$	$0.26\ (\pm 0.02, ^{+0.04}_{-0.01})$	$0.10\ (\pm 0.10, ^{+0.01}_{-0.09})$	0.09 ± 0.09	kT_1	0.60 ± 0.02
N_1	3.7 ± 0.1	4.9 ± 0.3	$1.7\ (\pm 0.1, ^{+0.1}_{-0.3})$	$2.7\ (\pm 0.6, ^{+0.1}_{-0.7})$	$0.3\ (^{+37.3}_{-0.2}, ^{+180.0}_{-0.1})$	$0.7^{+0.5}_{-0.6}$	N_1	3.7 ± 0.2
Z or $A_{\rm Rest}$	0.061 ± 0.006	0.10 ± 0.04	$0.28\ (\pm 0.04, ^{+0.08}_{-0.01})$	$0.15\ (^{+0.11}_{-0.08}, ^{+0.05}_{-0.08})$	$0.31\ (\pm 0.06, ^{+0.70}_{-0.01})$	$0.143^{+0.08}_{-0.05}$	Z	0.048 ± 0.006
kT_2			$0.94\ (\pm 0.03, ^{+0.05}_{-0.01})$	$0.96\ (\pm 0.05, \pm 0.04)$	$0.27\ (\pm 0.02, \pm 0.07)$	$0.26^{+0.03}_{-0.06}$	E_{G1}	0.58 ± 0.02
N_2			$1.1\ (\pm 0.1, ^{+0.1}_{-0.2})$	$1.6\ (\pm 0.3, ^{+0.1}_{-0.3})$	$1.5\ (\pm 0.2, ^{+0.1}_{-0.2})$	$1.5^{+0.5}_{-0.7}$	N_{G1}	0.03 ± 0.02
kT_3					$0.95\ (\pm 0.03, ^{+0.05}_{-0.01})$	$0.63^{+0.09}_{-0.04}$	E_{G2}	0.652 ± 0.009
N_3					$1.0\ (\pm 0.1, ^{+0.1}_{-0.2})$	$2.6^{+0.4}_{-0.8}$	N_{G2}	0.05 ± 0.01
$A_{\rm O}$		$0.12^{+0.04}_{-0.03}$		$0.16\ (\pm 0.06, ^{+0.08}_{-0.01})$		$0.18^{+0.09}_{-0.05}$	E_{G3}	0.920 ± 0.007
$A_{\rm Ne}$		0.47 ± 0.03		$0.2\ (\pm 0.1, ^{+0.2}_{-0.1})$		0.7 ± 0.2	N_{G3}	0.06 ± 0.01
$A_{\rm Si}$		0.3 ± 0.1		$0.1\ (\pm 0.1, ^{+0.2}_{-0.1})$		0.18 ± 0.10	E_{G4}	1.020 ± 0.007
$A_{\rm Fe}$		0.041 ± 0.008		$0.20\ (\pm 0.02, ^{+0.02}_{-0.06})$		0.07 ± 0.02	N_{G4}	0.047 ± 0.007
χ^2_ν ($\frac{\chi^2}{\rm d.o.f.}$)	$2.12(\frac{531.65}{251})$	$1.03(\frac{255.33}{247})$	$0.93(\frac{231.50}{249})$	$0.92(\frac{225.19}{245})$	$0.91(\frac{224.58}{247})$	$0.84(\frac{202.24}{243})$	χ^2_ν ($\frac{\chi^2}{\rm d.o.f.}$)	$0.93(\frac{225.16}{243})$
AIC	537.65	269.33	241.50	243.19	238.58	224.24	AIC	247.16
BIC	548.26	294.09	259.20	275.03	263.34	264.15	BIC	286.07

Notes. The normalisation $N_{\rm apec}$ is in the unit $10^{-4}\frac{10^{-14}}{4\pi(10{\rm pc})^2}$ cm^{-5}. The set of abundances is bonded for all components of a model. The error reported corresponds to 90 % confidence, assuming chi-squared statistics. In the models 2T-APEC, 2T-VAPEC, and 3T-APEC, the second error is the 90% confidence interval from the bootstrap re-sampling distribution (Appendix E). $A_{\rm element} = \frac{(n_Z/n_H)_{\rm plasma}}{(n_Z/n_H)_\odot}$. The 2T-APEC model was selected to model the flux.

6.1. Single-temperature plasma models

The single temperature APEC model yielded a poor fit (χ^2_ν = 2.12) with $kT = 0.66 \pm 0.02$ keV and an unusually low abundance of $Z_{\rm all} = 0.061 \pm 0.006\,Z_\odot$, which is lower than the typical values found in stellar coronae: $Z \approx 0.3$–$0.4\,Z_\odot$ (e.g. Favata et al. 2004, and Robrade & Schmitt 2005).

This is likely a spectral modelling bias related to stacking, similar to the 'artificial Fe bias' reported in studies of galaxy group and cluster, where a multi-temperature plasma (with different thermal components) was modelled using a single-temperature APEC model (Buote 2000; Sanders & Fabian 2011).

Residuals at 0.5–0.7 keV and 0.9–1.1 keV align with known strong emission lines, such as O VII, O VIII, Ne IX, and Ne X. This is demonstrated by the improved fit obtained by adding four Gaussian components at energies close to those of the brightest emission lines. In addition, treating the normalizations of the added Gaussian components as line intensities, we derived the O VIII/O VII ratio (blue dotted lines) and Ne X/Ne IX (red dotted lines). Those ratios, however, were inconsistent with theoretical ratios expected from a single temperature plasma, as shown in the right panel of Figure 4. This hinted at the need for an additional temperature component.

6.2. Multi-temperature plasma models

A dual-temperature APEC model (2T-APEC: χ^2_ν = 0.93) provided a significant improvement over the single-temperature APEC model and performed better than the single VAPEC model, as indicated by the F-test (see Table 3) and the AIC and BIC criteria. This suggests that the improvement in the fit is primarily driven by the inclusion of a second thermal component rather than by adjustments to the elemental abundances. The two plasma temperatures are $kT_1 = 0.27 \pm 0.01$ keV and $kT_2 = 0.94 \pm 0.03$ keV, with a tied abundance of $Z_{\rm all} = 0.28 \pm 0.04$. Though it is a relatively good fit, the residuals in the upper left panel of Figure 5 show the presence of a significant excess below 0.3 keV and a bump near 1.9 keV.

Adding a third temperature component (3T-APEC: χ^2_ν = 0.91) further improved the fit (see F test in Table 3; see AIC and BIC in Table 2). The additional cooler component has a poorly constrained temperature and normalization: $kT_1 = 0.1 \pm 0.1$ keV and $N_1 = 0.3^{+37.3}_{-0.2}$. From the upper left panel in Figure 5, we can see this component contributes only a tiny range of energies to the spectrum (<0.3 keV), effectively coming up (only) for the low-energy excess seen in the 2T-APEC model. In fact, the fitted temperatures of the second and third components are consistent with those obtained in the 2T-APEC model. Adding this component yields only a modest improvement, and the F test does not support it as statistically significant (p value=0.024).

We further applied 2T- and 3T-VAPEC models, with the elemental abundances linked between the two or three components. As mentioned in Sect. 5, the abundances of elements O, Ne, Si, and Fe were allowed to vary freely, while all other elements were tied together to vary. According to the statistical estimators, the 2T-VAPEC model (χ^2_ν = 0.92) provided a comparably good fit to that of the 2T-APEC model, but it requires four additional free parameters, making it the less favoured choice.

The 3T-VAPEC model (χ^2_ν = 0.84) appeared mildly overfitted, requiring an additional third component at a very soft temperature of 0.09 ± 0.09 keV, which is not constrained at all. Varying the elemental abundances alone does not resolve the soft excess and only shuffles the relative strength of the elements or components of the fit (see Appendix D).

This poorly constrained, very soft component is atypical for M stars and may instead reflect calibration uncertainties at the lowest energies. After updating to the most recent response files, calibrated using soft neutron-star spectra, its significance is already reduced compared to the previous version. We therefore restricted the subsequent analysis to two-temperature models and adopted the 2T-APEC model as our baseline. This model provides a simple description while retaining the key feature that its two components at 0.27 keV and 0.96 keV are also consistently required in the 2T-VAPEC and 3T-APEC models. We used the 2T-APEC model as the best fit for the following sub-group analysis of the M-star sample.

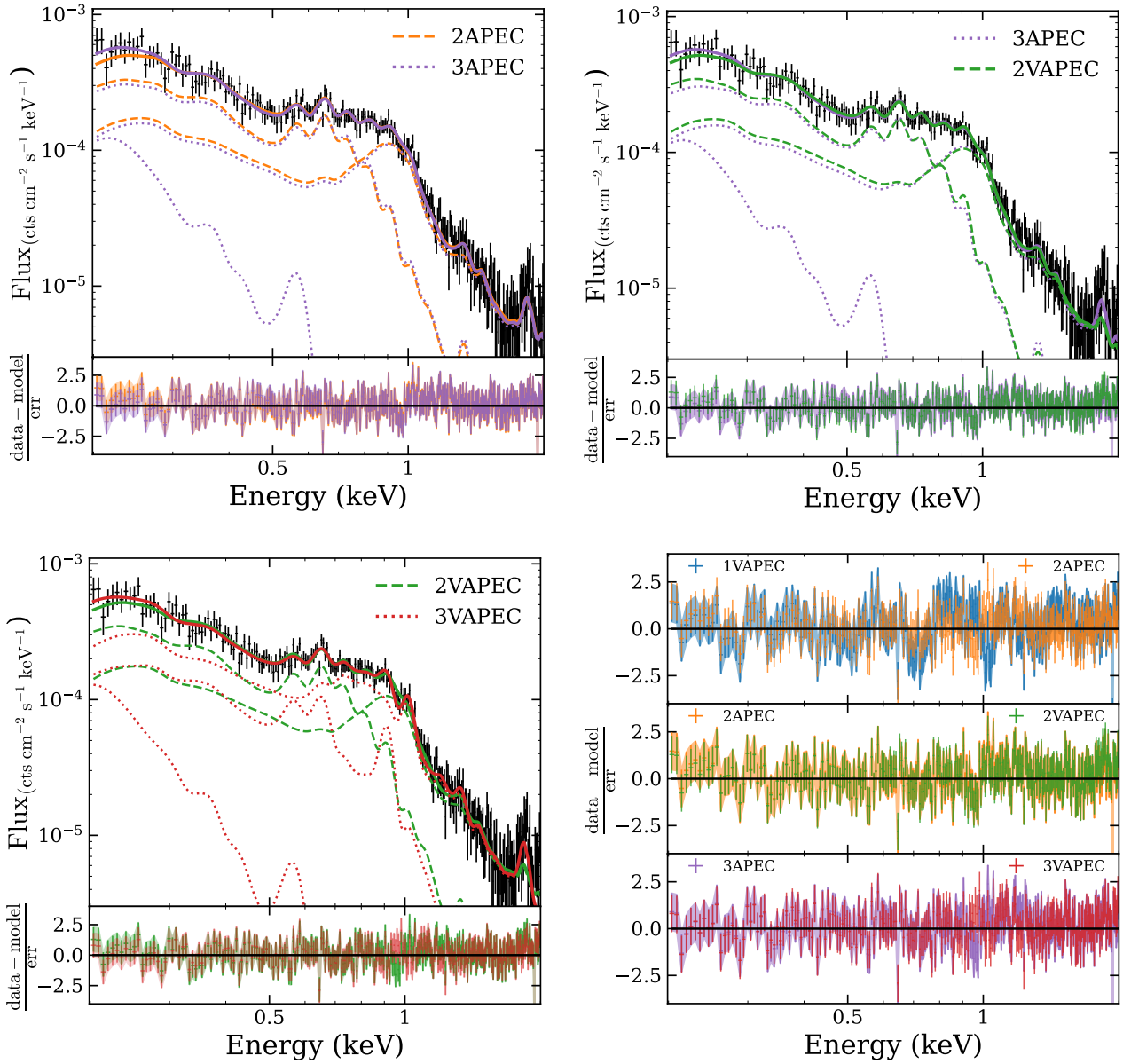

Fig. 5. Model fitting of the averaged X-ray spectra (0.2–2.0 keV) of 103 M-dwarf stars using multi-temperature thermal plasma models. The top left, top right and bottom left panels show comparisons between two-temperature and three-temperature APEC models (labelled as 2APEC and 3T-APEC), and as variable-abundance counterparts (2T-VAPEC and 3T-VAPEC). The corresponding residuals are shown. The bottom right panel presents a comparative view of residuals amongst four models to assess the fit quality.

6.3. Luminous M dwarfs versus the remaining sample

The X-ray-luminous stars potentially skew the spectral characteristics from the average spectral shape. In this section, we examined how AD Leonis and other very luminous stars affect the features of stacked average spectra. As shown in the left panel of Figure 1, AD Leo (AD Leo or BD+20 2465) stands out as the most luminous in our sample, lying near the upper envelope of the luminosity distribution. Although its colour corresponds to an early-M type (M3.5V), its X-ray luminosity is nearly an order of magnitude higher than that of typical M0–M4 stars, which is consistent with its well-known status as a magnetically active flare star (Stelzer et al. 2022). Following AD Leo are YZ CMi and G 41-14 AB, which are themselves about two times more luminous than AP Col. We therefore defined these four brightest M stars as the M4L group. Hence, we define two groups of stars: AD Leo to the remaining 102 M dwarfs with lower luminosity (M102R), and the four most luminous M stars (M4L) with the remaining 99 less luminous M stars (M99R).

Figure 6a shows the average X-ray spectra of the four groups, with the best-fit models from Table 4 overlaid. The 2T-APEC model was applied to the data over 0.2–2.5 keV, a broader range than in the other analysis of this work, to examine the harder spectrum that is expected for active stars. The average spectrum of M102R was scaled up by a factor of 30 to match the distance-normalised flux of AD Leo at 0.7 keV, while the M4L spectrum was scaled down by a factor of 20 to align with the flux of M99L at the same energy. From the ratio panel in the bottom of Figure 6a (flux normalised at 0.7 keV), we observed that AD Leo closely resembles M102R in the intermediate energy range (0.3–0.9 keV). The deviations increase at higher energies (>0.9 keV) and AD Leo exhibits overall harder spectrum. A similar trend is seen for M4L when compared with M99R.

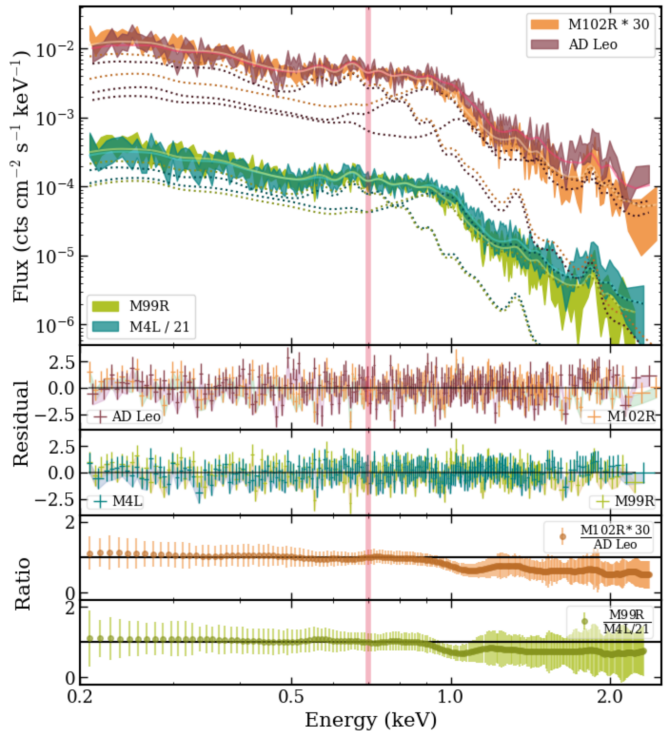

(a) AD Leo (brown) and the average fainter 102 M stars (M102R: orange), bright 4 M stars (M4L: blue), and fainter 99 M stars (M99R: green). The 0.2–2.5 keV range was considered for model fitting.

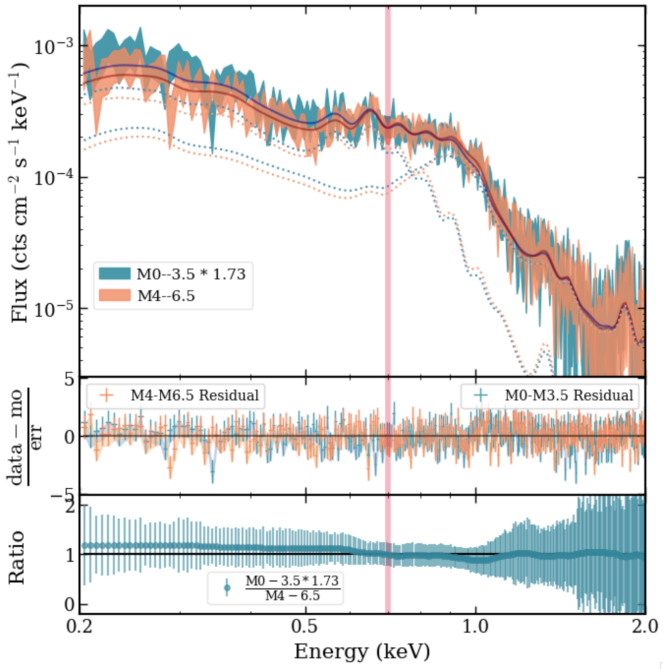

(b) Average spectra of 57 early-type M stars (M0–M3.5: blue) and the 44 M mid-late-type stars (M4–M6.5: orange). The 0.2–2.0 keV range was considered for model fitting.

Fig. 6. Comparison between X-ray brightness sub-groups and sub-spectral-type groups. All spectra are normalised to a distance of 10 pc and aligned at 0.7 keV for comparison. Each spectrum is fitted with a 2T-APEC model. The residual ($\frac{\text{data}-\text{model}}{\text{error}}$) from fit and the ratio between the two spectra is shown.

Table 3. F-test statistics of models for average M star.

Simpler Model	More complex Model	Δ d.o.f.	$\Delta\chi^2$	F-value	p-value
1T-APEC	2T-APEC	2	300.15	161.4	1×10^{-45}
2T-APEC	3T-APEC	2	6.92	3.8	0.024
1T-APEC	1T-VAPEC	4	276.32	66.8	3×10^{-38}
2T-APEC	1T-VAPEC	2	–23.83	<0	–
2T-APEC	2T-VAPEC	4	23.69	1.7	0.14
3T-APEC	2T-VAPEC	2	–0.61	<0	–
3T-APEC	3T-VAPEC	4	22.34	6.7	4×10^{-5}
1T-VAPEC	2T-VAPEC	2	30.14	16.4	2×10^{-7}
2T-VAPEC	3T-VAPEC	2	22.95	13.8	2×10^{-6}

Notes. The improvement in best fit between two models regarding change in degrees of freedom (Δ d.o.f.), change in χ^2, the corresponding F value, and the resulting p value. The d.o.f. is $N_{\text{data}} - N_{\text{free param.}}$.

Table 4. Fitting parameters for different luminosity groups.

Param.	99 lower luminosity	102 lower luminosity	4 higher luminosity	AD Leo (at 10 pc)
kT_1	0.27 ± 0.02	0.27 ± 0.01	0.28 ± 0.02	0.26 ± 0.01
N_1	1.3 ± 0.1	1.5 ± 0.1	20 ± 3	25 ± 5
kT_2	0.92 ± 0.04	0.93 ± 0.03	$1.03^{+0.05}_{-0.06}$	$0.94^{+0.08}_{-0.11}$
N_2	0.8 ± 0.1	1.0 ± 0.1	19 ± 4	16^{+7}_{-5}
kT_3				$1.5^{+0.7}_{-0.3}$
N_3				15^{+7}_{-5}
$Z/Z_\odot$	$0.24^{+0.05}_{-0.04}$	$0.26^{+0.05}_{-0.04}$	$0.29^{+0.09}_{-0.07}$	$0.5^{+0.2}_{-0.1}$
χ^2_ν	$0.6\ (\frac{132.73}{210})$	$0.8\ (\frac{178.69}{224})$	$0.4\ (\frac{83.24}{202})$	$1.3\ (\frac{255.12}{201})$
$L_{0.2\text{-}2.5}$	1.81 ± 0.05	2.26 ± 0.05	39 ± 1	73 ± 2

Notes. Fitting was done for spectra in the 0.2–2.5 keV range. The 3T-APEC model was used for AD Leo as it was essential. All spectra were normalised to 10 pc and binned to a minimum of ten counts per channel. N_{apec} is in unit of $10^{-4}\frac{10^{-14}}{4\pi(10\text{pc})^2}$ cm^{-5}. Luminosities are given in 10^{27}erg/s unit. A 90% chi-squared statistics error is shown.

The best-fitting parameters are listed in Table 4. The average spectra of M99R, M102R, and M4L are well described by two components with temperatures of ~0.27 and 0.92–1.03 keV, yielding good fits with $\chi^2_\nu < 0.8$ that indicate slight over-fitting. The fits for spectra of AD Leo were fitted with components at 0.26, 0.94, and 1.5 keV. The fitting of AD Leo is marginally acceptable: χ^2_ν=1.3. The residuals scatter at 0.45–0.6 keV.

The M102R, M99R, and M4L samples have remarkably consistent best-fitting parameters (T and Z) in relation to each other and with the whole M-star sample in Table 2. All spectra share a consistent intermediate-temperature component (~0.27 keV) and hotter components at (~0.9 keV). Those two contribute the majority of the emission. Only AD Leo exhibits an additional high-temperature component around 1.5 keV and higher coronal abundances ($0.5^{+0.2}_{-0.1}$) compared to the rest of the groups. The relatively poor fit of AD Leo may reflect its distinct magnetic

Table 5. Fitting parameters for average spectra of M0–M3.5 and M4–M6.5 sub-groups.

Param.	[M0-M3.5]	[M4-M6.5]
kT_1	0.26 ± 0.02	0.27 ± 0.01
N_1	1.5 ± 0.2	1.9 ± 0.3
kT_2	0.92 ± 0.05	0.96 ± 0.04
N_2	0.9 ± 0.2	1.3 ± 0.2
$Z/Z_\odot$	$0.24^{+0.06}_{-0.05}$	$0.34^{+0.08}_{-0.06}$
$\chi^2_\nu(\frac{\chi^2}{\text{d.o.f.}})$	$0.82\ (\frac{205.21}{249})$	$0.74\ (\frac{183.69}{249})$
$L_{0.2\text{-}2.0}$	2.03 ± 0.06	3.34 ± 0.09

Notes. Fitting was done for spectra in the 0.2–2.0 keV range. Same treatment and denotation as Table 4 is applied.

activity that is not fully captured at the current energy resolution. Despite its individual peculiarities, both AD Leo's and M4L's overall spectral shapes remain broadly similar to those of other M dwarfs in the central energy range. By comparing with the best fit of all M stars in Table 2, we conclude that either excluding AD Leo or the four most luminous stars from the stacked sample, does not significantly alter any parameter except for the overall normalisation.

6.4. Early-type M dwarfs versus late-type M dwarfs

The structural differences between early-type and late-type M dwarfs are particularly relevant for analysing their X-ray spectral properties. Early-type M dwarfs possess a radiative core, whereas mid- and late-type M dwarfs are fully convective. This can influence their X-ray emission characteristics, which may be obscured if the two groups are combined in the analysis.

To investigate this distinction, we divided the 10 pc sample of M dwarfs into M0–M3.5 (early-type) and M4–M6.5 (mid- and late-type) groups. For clarity and to minimise potential biases, we excluded a pair of M stars, CD –37 10765 A (M3V) and B (M5V), which belong to different sub-spectral-type groups and are not distinguishable in X-rays. The final sample comprises 57 stars of sub-type M0–M3.5 and 44 stars of sub-type M4–M6.5, with two stars excluded.

Figure 6b presents the X-ray spectra of the two groups; M0–M3.5 exhibit lower flux than M4–6.5 in the studied energy range; hence, we scaled up the flux of the M0–M3.5 group by a factor of 1.73 to match the flux of the M4–M6.5 group at 0.7 keV for comparison. The top panel shows the fit using the two-temperature 2T-APEC model (see also in Table 5), and the middle panel displays the residuals of the fits. The bottom panel of Figure 6b shows the ratio between the scaled spectrum of the M0–M3.5 group and that of the M4–M6.5 group.

By visual inspection, the spectra reveal overall consistency in spectral shape despite the different luminosities, especially in the 0.5–2.0 keV range from the ratio plot. The mismatch rises in the very soft (<0.5 keV) band as the early-type M dwarfs display a relatively softer flux than the mid- and late-type ones.

Table 5 summarises the spectral fits for M0–M3.5- and M4–M6.5-type M dwarfs using 3T-APEC models. Both fits achieve low reduced χ^2. The metal abundances are consistent between the two groups. The temperatures of the intermediate and hot components (kT_1 and kT_2) are in good agreement between the two groups. Interestingly, the M0–M3.5 stars in our sample are approximately 40% fainter in X-ray luminosity compared to their M4–M6.5 counterparts, contrary to conventional expectations. Early-type M dwarfs, in which a radiative core remains beneath their convective envelopes, are generally thought to sustain higher coronal temperatures and produce more energetic flares, leading to stronger X-ray emission, particularly at harder energies. Late-type M dwarfs, on the other hand, are fully convective and often exhibit saturated magnetic activity. While this can maintain a high X-ray luminosity relative to their bolometric output, they are not usually expected to surpass earlier types in absolute luminosity due to $L_X - M_*$ dependence (see e.g. Magaudda et al. 2022; Magaudda et al. 2020). The observed trend suggests that additional effects, such as sample selection biases or flare activity, may contribute to the emission. It would therefore be valuable to test the luminosity–spectral-type relation with larger samples and assess whether the 10-pc stars are systematically different from the common Galactic population.

7. Results: F-, G-, and K-type star sample

In this section, we describe how we applied the same spectral fitting approach used for the M dwarfs to the stacked spectra of FGK-type stars within the 10-pc WGH sample. The spectrum shown in Figure 7 is constructed from 30 FGK-type dwarf stars, all included in the *eROSITA*_DE sky survey. While this dataset comprehensively measures nearby FGK-type stars, the limited sample size may not fully capture the diversity of coronal properties present within this stellar class. FGK dwarfs are brighter than M dwarfs in the optical and ultraviolet bands. A high optical and UV brightness potentially introduces optical loading on the SRG/eROSITA detectors. This effect alters the information on the detected photons (number, energy, and detection pattern) and becomes increasingly important at lower energies. In fact, a significant number of these FGK stars are potentially affected by optical loading. To retain all 30 FGK-type stars in the analysis, we restricted our spectral fitting to energies above 0.35 keV. By doing so, we mitigated the influence of optical loading, whose effect is only significant at lower energies (see Appendix A). We note that this treatment largely helped to reduce the flux excess at the soft end; however, it is important to note that the blueshift caused by optical loading affects the entire energy range. We present spectra affected by and free from optical loading below 0.35 keV in Appendix A, and we tested them with the 3T model.

The parameters obtained from all fitted models are summarised in Table 6. Similarly to the M-dwarf case, the fit using a single-temperature APEC model (1T-APEC) yields statistically unacceptable results, with a reduced chi-squared of $\chi^2_\nu = 2.58$. The same considerations are valid when adding complexity to this simple model. We thus do not discuss this model further. The 1T-VAPEC model, which allows metal abundances to vary, also provides a poor fit with $\chi^2_\nu = 1.94$. Together with the inadequate fit of the 1T-APEC model, this result suggests that a single-temperature description is insufficient—even when elemental abundances are allowed to vary. Therefore, we added a second APEC model (2T-APEC; top left panel in Figure 7), which significantly improved the fit, reducing the chi-squared by $\Delta\chi^2 = 225.35$ for two additional d.o.f. (see Table 6).

The 2T-VAPEC model further improves the fit compared to both the 1T-VAPEC model and the 2T-APEC model in relation to the F test (see Table 7). The best-fit temperatures for the two components are 0.22 ± 0.01 keV and 0.60 ± 0.02 keV, with corresponding abundances of $A_{\rm O} = 0.14^{+0.06}_{-0.04}$, $A_{\rm Ne} = 0.8^{+0.3}_{-0.2}$, $A_{\rm Si} = 0.18^{+0.12}_{-0.09}$, and $A_{\rm Fe} = 0.27^{+0.09}_{-0.06}$, and a shared abundance of $0.3^{+0.2}_{-0.1}$ for the rest of the elements.

Instead of leaving the metal abundances free to vary, another way to add complexity with respect to the 2T-APEC model is

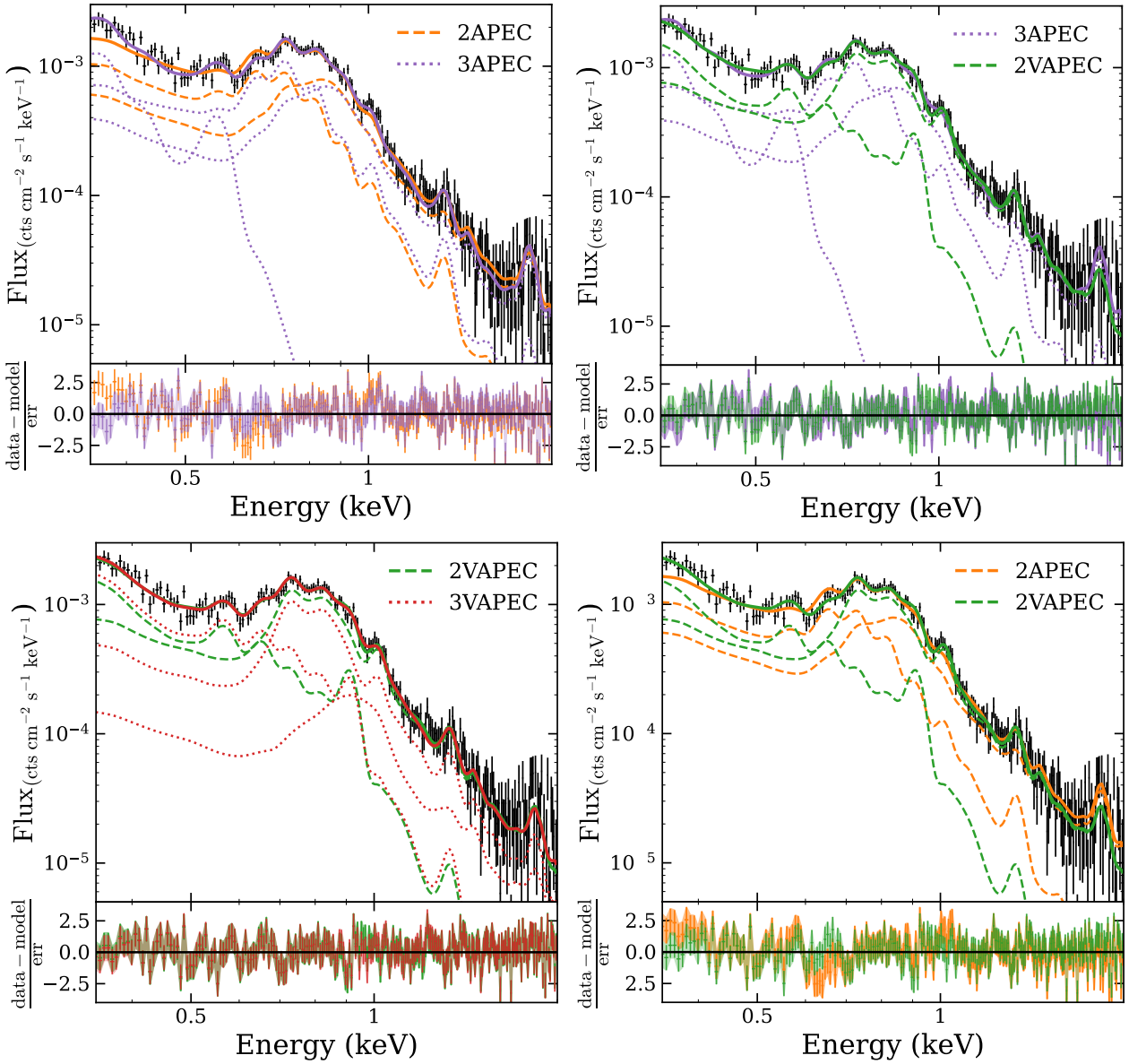

Fig. 7. Model fitting of averaged X-ray spectra of 30 FGK stars (0.35–2.0 keV) using multi-temperature thermal plasma models. The four panels compare the performance of two-temperature and three-temperature APEC and VAPEC models, with corresponding residuals shown below each spectrum. The corresponding residuals are shown.

to introduce a third thermal component (with linked abundance across all components). This 3T-APEC fit ($\chi^2_\nu = 1.15$) also shows improvement relative to the 2T-APEC model. The F-test comparison, $F(2, 96.36)$, also supports the 3T-APEC model over the 2T-APEC configurations. The best-fit temperatures from the 3T-APEC model are $kT_1 = 0.09 \pm 0.01$ keV, $kT_2 = 0.35 \pm 0.02$ keV, and $kT_3 = 0.79 \pm 0.03$ keV, with a shared abundance of $0.55^{+0.13}_{-0.09}$. The presence of the very soft component ($kT_1 = 0.09 \pm 0.01$) could be a residual effect of optical loading.

An F test comparing the 2T-VAPEC and 3T-APEC fits yields (F(2,17.61)=8.1), exceeding the 3σ threshold and favouring 2T-VAPEC over 3T-APEC. This indicates that improving the 2T-APEC description by allowing metal abundances to vary is more effective than adding an extra thermal component. At the same time, while 3T-VAPEC improves upon 3T-APEC, it does not outperform 2T-VAPEC: the comparison between 3T-VAPEC and 2T-VAPEC gives (F(2,5.77)=2.7) (p = 0.069), below 3σ significance. Considering ΔAIC and ΔBIC alongside the F tests, we adopted 2T-VAPEC as the conservative model for the subsequent discussion.

Although this analysis includes all FGK stars within the 10-pc WGH, the limited sample size may not provide a sufficiently comprehensive spectroscopic view of the unified properties of local FGK stars. Further studies employing higher resolution spectra and/or larger samples will be essential to refine these preliminary findings, especially regarding the softest end of the energy band considered here.

8. Results: Average luminosities

In Table 8, we report the flux and luminosity in different energy bands for the eROSITA_DE stacked 10 pc (WGH) M-dwarf spectrum based on the 2T-APEC and 2T-VAPEC models. The flux from component 0.27 keV and 0.94 keV is reported in

Table 6. Model parameters and values for F-, G-, and K-dwarf-averaged spectra.

Param.	APEC	VAPEC	2T-APEC	2T-VAPEC	3T-APEC	3T-VAPEC		APEC+GAUSS
kT_1	0.56 ± 0.01	$0.42^{+0.02}_{-0.01}$	$0.31\ (\pm 0.02, \pm 0.02)$	$0.22\ (\pm 0.01, ^{+0.02}_{-0.01})$	$0.09\ (\pm 0.01, \pm 0.01)$	$0.23\ (\pm 0.01, \pm 0.01)$	kT_1	0.51 ± 0.01
N_1	17.0 ± 0.7	24 ± 2	$8.0\ (\pm 0.9, ^{+2.6}_{-0.1})$	$10\ (\pm 2, \pm 2)$	$10\ (^{+5}_{-3}, ^{+1}_{-3})$	$9\ (\pm 3, ^{+3}_{-2})$	N_1	17.4 ± 0.9
Z *or* $A_{\rm Rest}$	0.14 ± 0.01	0.14 ± 0.04	$0.31\ (\pm 0.04, ^{+0.06}_{-0.02})$	$0.3\ (^{+0.2}_{-0.1}, ^{+0.2}_{-0.1})$	$0.55\ (^{+0.13}_{-0.09}, ^{+0.18}_{-0.06})$	$0.4\ (^{+0.4}_{-0.2}, ^{+0.4}_{-0.1})$	Z	0.13 ± 0.01
kT_2			$0.75\ (\pm 0.03, ^{+0.05}_{-0.01})$	$0.60\ (\pm 0.02, \pm 0.02)$	$0.35\ (\pm 0.02, \pm 0.01)$	$0.59\ (^{+0.06}_{-0.07}, ^{+0.04}_{-0.09})$	E_{G1}	0.57 ± 0.01
N_2			$5.5\ (^{+0.8}_{-0.7}, ^{+1.0}_{-0.1})$	$8\ (\pm 2, ^{+4}_{-1})$	$4.6\ (\pm 0.8, ^{+1.8}_{-0.1})$	$5\ (^{+3}_{-2}, ^{+3}_{-2})$	N_{G1}	0.11 ± 0.07
kT_3					$0.79\ (\pm 0.03, ^{+0.04}_{-0.01})$	$1.0\ (^{+0.1}_{-0.2}, ^{+0.1}_{-0.3})$	E_{G2}	0.65 (fixed)
N_3					$3.1\ (\pm 0.6, ^{+0.9}_{-0.3})$	$1.5\ (^{+1.5}_{-0.9}, ^{+2.5}_{-0.8})$	N_{G2}	0.02 ± 0.02
$A_{\rm O}$		0.06 ± 0.03		$0.14\ (^{+0.06}_{-0.04}, ^{+0.08}_{-0.02})$		$0.19\ (^{+0.14}_{-0.07}, ^{+0.15}_{-0.06})$	E_{G3}	$0.915^{+0.009}_{-0.007}$
$A_{\rm Ne}$		$0.44^{+0.06}_{-0.05}$		$0.8\ (^{+0.3}_{-0.2}, ^{+0.4}_{-0.1})$		$0.7\ (^{+0.4}_{-0.3}, ^{+0.5}_{-0.2})$	N_{G3}	0.35 ± 0.05
$A_{\rm Si}$		$0.22^{+0.09}_{-0.08}$		$0.18\ (^{+0.12}_{-0.09}, ^{+0.01}_{-0.18})$		$0.2\ (^{+0.2}_{-0.1}, ^{+0.1}_{-0.2})$	E_{G4}	1.01 ± 0.01
$A_{\rm Fe}$		$0.12^{+0.02}_{-0.01}$		$0.27\ (^{+0.09}_{-0.06}, ^{+0.08}_{-0.06})$		$0.4\ (^{+0.3}_{-0.1}, ^{+0.3}_{-0.1})$	N_{G4}	0.14 ± 0.03
$\chi^2_\nu\ (\frac{\chi^2}{\rm d.o.f.})$	$2.58\ (\frac{574.48}{223})$	$1.94\ (\frac{424.11}{219})$	$1.58\ (\frac{349.13}{221})$	$1.08\ (\frac{235.16}{217})$	$1.15\ (\frac{252.77}{219})$	$1.07\ (\frac{229.39}{215})$	$\chi^2_\nu\ (\frac{\chi^2}{\rm d.o.f.})$	$1.49\ (\frac{321.25}{216})$
AIC	580.48	438.11	359.13	253.16	266.77	251.39	AIC	341.25
BIC	590.74	436.53	376.23	283.94	290.71	289.01	BIC	375.46

Notes. The fit was conducted in a 0.35–2.0 keV energy range. Normalisation, $N_{\rm apec}$, is in the unit $10^{-4}\,\frac{10^{-14}}{4\pi(10{\rm pc})^2}\ {\rm cm}^{-5}$. The set of abundance is bonded for all components of a model. The error reported corresponds to 90% confidence, assuming chi-squared statistics. In 2T-VAPEC, 3T-APEC, and 3T-VAPEC, the second error is the 90% confidence interval from the bootstrap resampling distribution (Appendix E): $A_{\rm element} = \frac{(n_Z/n_H)_{\rm plasma}}{(n_Z/n_H)_\odot}$.

Table 7. F-test statistics of models for the average FGK star.

Simpler Model	More complex Model	Δ d.o.f.	$\Delta\chi^2$	F-value	p-value
1T-APEC	2T-APEC	2	225.35	71.3	1×10^{-24}
2T-APEC	3T-APEC	2	96.36	41.7	4×10^{-16}
1T-APEC	1T-VAPEC	4	150.37	19.4	1×10^{-13}
2T-APEC	1T-VAPEC	2	-74.98	<0	–
2T-APEC	2T-VAPEC	4	113.97	26.3	9×10^{-18}
3T-APEC	2T-VAPEC	2	17.61	8.1	4×10^{-4}
3T-APEC	3T-VAPEC	4	23.38	5.5	3×10^{-4}
1T-VAPEC	2T-VAPEC	2	188.95	87.2	2×10^{-28}
2T-VAPEC	3T-VAPEC	2	5.77	2.7	0.069

Notes. The improvement in best-fit between two models regarding change in degrees of freedom (Δ d.o.f.), change in χ^2, the corresponding F value, and the resulting p value. The d.o.f. is $N_{\rm data} - N_{\rm free\ param.}$.

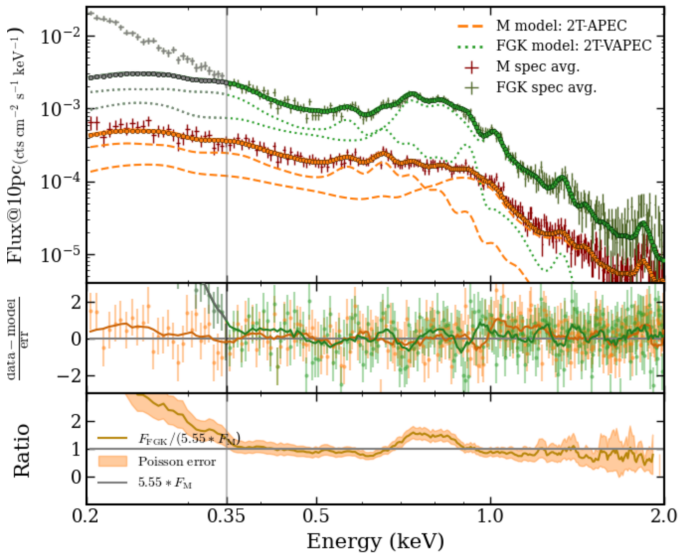

Fig. 8. Comparison of spectra of 103 M stars (orange) and 30 FGK stars (green) in the 10-pc *Gaia* sample. Models 2T-apec and 2T-VAPEC were applied, respectively. The middle panel displays the residual of the fit. The bottom panel shows the ratio between the average FGK and 5.55 times brighter M-star spectra. The scale comes from the ratio of luminosity in 0.2–2.0 keV. The Poisson noise is applied.

0.2–2.0 keV and extrapolated for 0.1–2.4 keV, which is the band pass of the ROSAT PSPC. We also derived FGK average luminosities for the 2T-VAPEC and 3T-VAPEC models in Table 9. We define and report conservative uncertainties for flux and luminosity by accounting for the differences between the AC and AR stacking methods. Specifically, the quoted uncertainties were taken as the envelope (union) of the 90% χ^2 statistical confidence and intervals and the systematic offset between results produced by the AC and AR methods. This provides a lower bound on the total uncertainty compared to that derived from model fitting.

In the 0.2–2.0 keV band, M dwarfs exhibit an average luminosity of $(2.6 \pm 0.1) \times 10^{27}$ erg s^{-1} (2T-APEC), while FGK stars have $(15 \pm 3) \times 10^{27}$ erg s^{-1} (2T-VAPEC). Thus, the averaged FGK star in 10 pc (WGH) is more than five times brighter than an M dwarf in this energy range. In Figure 8, we present the spectra of M stars and FGK stars overlaid with their respective model fits. By comparing the M-star and FGK-star spectra in the bottom panel of Figure 8, we find the overall similarity, except the primary difference arising in the 0.7–0.9 keV energy range. In Figure F.1, we also show that there is no significant systematic variation in the average luminosity is observed across the four eRASS epochs.

Independent of the ten-WGH sample considered in this work, early-type M stars (M0–M4) in the EGH appear to host more high-luminosity sources than the WGH. Across the combined WGH+EGH 10-pc *Gaia* sample, M dwarfs can exhibit a mean luminosity of up to $\sim 6 \times 10^{27}$ erg s^{-1}, as inferred from Caramazza et al. (2023). By comparison, the FGK sample shows no measurable hemispheric dependence in its average luminosity.

Table 8. Fluxes and luminosities of stacked M-star spectra.

Model	Energy range (keV)	Flux@10 pc (10^{-13} erg/cm^2/s)	Luminosity (10^{27} erg/s)
2T-APEC	0.2–2.0	2.2 ± 0.1	2.6 ± 0.1
	0.2–0.5	0.74 ± 0.04	0.9 ± 0.1
	0.5–1.0	1.06 ± 0.03	1.27 ± 0.04
	1.0–2.0	0.39 ± 0.02	0.46 ± 0.02
	0.1–2.4	2.7 ± 0.1	3.2 ± 0.1
T_1(0.27 keV)	0.2–2.0	1.08 ± 0.08	1.3 ± 0.1
	0.1 – 2.4	1.4 ± 0.1	1.7 ± 0.1
T_2(0.94 keV)	0.2–2.0	1.11 ± 0.07	1.33 ± 0.08
	0.1–2.4	1.33 ± 0.08	1.6 ± 0.1
2T-VAPEC	0.2–2.0	2.2 ± 0.1	2.6 ± 0.1
	0.2–0.5	0.76 ± 0.08	0.9 ± 0.1
	0.5–1.0	1.06 ± 0.05	1.26 ± 0.05
	1.0–2.0	0.38 ± 0.03	0.46 ± 0.03
	0.1–2.4	2.7 ± 0.1	3.3 ± 0.2
T_2(0.26 keV)	0.2–2.0	1.11 ± 0.08	1.3 ± 0.1
	0.1–2.4	1.4 ± 0.1	1.7 ± 0.1
T_3(0.96 keV)	0.2–2.0	1.09 ± 0.04	1.3 ± 0.05
	0.1–2.4	1.31 ± 0.05	1.57 ± 0.05

Table 9. Fluxes and luminosities of stacked FGK-star spectra.

Model	Energy range (keV)	Flux@10 pc (10^{-13} erg/cm^2/s)	Luminosity (10^{27} erg/s)
2T-VAPEC	0.2–2.0	13 ± 2	15 ± 3
	0.2–0.5	4.5 ± 0.9	5 ± 1
	0.5–1.0	6 ± 2	8 ± 2
	1.0–2.0	1.8 ± 0.9	2.2 ± 0.8
	0.1–2.4	16 ± 4	19 ± 4
T_1(0.22 keV)	0.2–2.0	5 ± 1	6 ± 1
	0.1–2.4	7 ± 1	8 ± 1
T_2(0.60 keV)	0.2–2.0	8 ± 2	9 ± 2
	0.1–2.4	9 ± 1	11 ± 2
3T-VAPEC	0.2–2.0	13 ± 2	15 ± 3
	0.2–0.5	4.4 ± 0.8	5 ± 1
	0.5–1.0	7 ± 1	8 ± 2
	1.0–2.0	1.8 ± 0.4	2.1 ± 0.6
	0.1–2.4	16 ± 3	19 ± 4
T_1(0.23 keV)	0.2–2.0	5.6 ± 0.7	6.7 ± 0.8
	0.1–2.4	7.4 ± 0.8	8.8 ± 0.9
T_2(0.59 keV)	0.2–2.0	6 ± 1	7 ± 2
	0.1–2.4	6 ± 2	8 ± 2
T_3(1.0 keV)	0.2–2.0	1.6 ± 0.5	2.0 ± 0.6
	0.1–2.4	1.9 ± 0.6	2.3 ± 0.7

Notes. The fluxes and luminosities were derived from the best-fit models of fitting spectra in 0.2–2.0 keV for M stars and 0.35–2.0 keV for FGK stars. For the 0.1–2.4 keV band, corresponding to the ROSAT band, the values were obtained by extrapolating these best-fit models. Fluxes are presented as if one average source were located at 10 pc. The uncertainties here are the conservative union of the 90% χ^2 statistical confidence intervals and the systematic offset between the AC and AR stacking methods.

9. Conclusions

In this study, we produced the highest signal-to-noise distance-normalised spectrum of M dwarfs and FGK-type stars by stacking over the volume-complete sample of stars within 10 pc in the western Galactic hemisphere, using data from the first four X-ray surveys of the sky performed by the SRG/*eROSITA* instrument (eRASS1 to 4). The average X-ray luminosity of WGH in 0.2–2.0 keV is of $(2.6 \pm 0.1) \times 10^{27}$ erg/s for 10 pc M-type stars, and $(15 \pm 3) \times 10^{27}$ erg/s for F-, G-, and K-type stars. When considering the entire 10-pc *Gaia* sample in both WGH and EGH, the average luminosity for the M star sample could be as high as $\sim 6 \times 10^{27}$ erg/s, cross-estimated from Caramazza et al. (2023), whereas the average luminosity of FGK stars shows no significant difference between the two hemispheres. The luminosities derived here are in good agreement across all four eRASS surveys. The stacked spectra are well reproduced by collisionally ionised plasma components at different temperatures. The fitted temperature structure and abundances remain consistent despite the presence of the most luminous outliers in the brightness distribution. Specifically, all M-star sub-samples tested exhibit the same two thermal components, at approximately 0.27 keV and 0.94 keV. Additional softer or harder components are required depending on the energy range considered and ongoing flaring activity. Apart from the emission measure, no evidence of systematic differences in the fitted parameters are found between the stacked spectra of early-type (M0–M3.5) and mid-to-late-type (M4–M6.5) M dwarfs. Interestingly, the early M stars appear on average less luminous than the mid- and late-M stars, in contrast to the expected L_X–M_* trend (Magaudda et al. 2022).

Our study provides insights into nearby low-mass stars' X-ray luminosity properties. In this work, we used the highest statistics from the four *eROSITA* All-Sky Surveys combined. Potential improvement may come from the availability of models to account for optical loading.

Data availability

The catalogue is available at the CDS via https://cdsarc.cds.unistra.fr/viz-bin/cat/J/A+A/709/A275

Acknowledgements. This work is based on data from eROSITA, the soft X-ray instrument aboard SRG, a joint Russian-German science mission supported by the Russian Space Agency (Roskosmos), in the interests of the Russian Academy of Sciences represented by its Space Research Institute (IKI), and the Deutsches Zentrum für Luft und Raumfahrt (DLR). The SRG spacecraft was built by Lavochkin Association (NPOL) and its subcontractors, and is operated by NPOL with support from the Max Planck Institute for Extraterrestrial Physics (MPE). The development and construction of the eROSITA X-ray instrument was led by MPE, with contributions from the Dr. Karl Remeis Observatory Bamberg & ECAP (FAU Erlangen-Nuernberg), the University of Hamburg Observatory, the Leibniz Institute for Astrophysics Potsdam (AIP), and the Institute for Astronomy and Astrophysics of the University of Tübingen, with the support of DLR and the Max Planck Society. The Argelander Institute for Astronomy of the University of Bonn and the Ludwig Maximilians Universität Munich also participated in the science preparation for eROSITA. The eROSITA data shown here were processed using the eSASS/NRTA software system developed by the German eROSITA consortium. We acknowledge financial support from the European Research Council (ERC) under the European Union's Horizon 2020 research and innovation program Hot-Milk (grant agreement No. 865637). GP acknowledges support from Bando per il Finanziamento della Ricerca Fondamentale 2022 dell'Istituto Nazionale di Astrofisica (INAF): GO Large program and from the Framework per l'Attrazione e il Rafforzamento delle Eccellenze

(FARE) per la ricerca in Italia (R20L5S39T9). MF and MY acknowledge support from the Deutsche Forschungsgemeinschaft through the grant FR 1691/2-1. W.B. acknowledges support from the Deutsche Forschungsgemeinschaft through the project BE 1649/11-1 and BE 1649/11-2 within the Research Unit FOR 2990 (eRO-STEP).

References

Akaike, H. 1974, IEEE Trans. Automatic Control, 19, 716
Arnaud, K. A. 1996, in Astronomical Society of the Pacific Conference Series, 101, Astronomical Data Analysis Software and Systems V, eds. G. H. Jacoby, & J. Barnes, 17
Asplund, M., Grevesse, N., Sauval, A. J., & Scott, P. 2009, ARA&A, 47, 481
Bensby, T., Feltzing, S., & Oey, M. S. 2014, A&A, 562, A71
Bochanski, J. J., Hawley, S. L., Covey, K. R., et al. 2010, AJ, 139, 2679
Brunner, H., Liu, T., Lamer, G., et al. 2022, A&A, 661, A1
Buote, D. A. 2000, ApJ, 539, 172
Caramazza, M., Stelzer, B., Magaudda, E., et al. 2023, A&A, 676, A14
Dennerl, K., Andritschke, R., Bräuninger, H., et al. 2020, SPIE Conf. Ser., 11444, 114444Q
Favata, F., Micela, G., Baliunas, S. L., et al. 2004, A&A, 418, L13
Golovin, A., Reffert, S., Just, A., et al. 2023, A&A, 670, A19
Güdel, M. 2004, A&A Rev., 12, 71
Ishikawa, K., Ezoe, Y., Ohashi, T., Kimura, T., & Miyoshi, Y. 2019, Proc. Int. Symp. Planet. Sci., 2011
Jofré, P., Heiter, U., Soubiran, C., et al. 2015, A&A, 582, A81
Kirkpatrick, J. D., Marocco, F., Gelino, C. R., et al. 2024, ApJS, 271, 55
Locatelli, N., Ponti, G., Magaudda, E., & Stelzer, B. 2025, A&A, 702, A237
Lumb, D. 2000, PHS Tools – EPIC Optical Loading
Magaudda, E., Stelzer, B., Covey, K. R., et al. 2020, A&A, 638, A20
Magaudda, E., Stelzer, B., Raetz, S., et al. 2022, A&A, 661, A29
Meidinger, N., Andritschke, R., Dennerl, K., et al. 2021, J. Astron. Telesc. Instrum. Syst., 7, 025004
Merloni, A., Predehl, P., Becker, W., et al. 2012, arXiv e-prints [arXiv:1209.3114]
Merloni, A., Lamer, G., Liu, T., et al. 2024, A&A, 682, A34
Mewe, R. 1991, A&A Rev., 3, 127
Montes, D., González-Peinado, R., Tabernero, H. M., et al. 2018, MNRAS, 479, 1332
Neves, V., Bonfils, X., Santos, N. C., et al. 2012, A&A, 538, A25
Parker, E. N. 1993, ApJ, 408, 707
Predehl, P., Andritschke, R., Arefiev, V., et al. 2021, A&A, 647, A1
Ramstedt, S., Montez, R., Kastner, J., & Vlemmings, W. H. T. 2012, A&A, 543, A147
Raymond, J. C., & Smith, B. W. 1977, ApJS, 35, 419
Reid, I. N., & Gizis, J. E. 1997, AJ, 113, 2246
Reylé, C., Jardine, K., Fouqué, P., et al. 2021, A&A, 650, A201
Robrade, J., & Schmitt, J. H. M. M. 2005, A&A, 435, 1073
Sanders, J. S., & Fabian, A. C. 2011, MNRAS, 412, L35
Schmitt, J. H. M. M., & Liefke, C. 2004, A&A, 417, 651
Schwarz, G. 1978, Ann. Statist., 6, 461
Smith, R. K., Brickhouse, N. S., Liedahl, D. A., & Raymond, J. C. 2001, ApJ, 556, L91
Stelzer, B., Caramazza, M., Raetz, S., Argiroffi, C., & Coffaro, M. 2022, A&A, 667, L9
Verner, D. A., Ferland, G. J., Korista, K. T., & Yakovlev, D. G. 1996, ApJ, 465, 487
Woolf, V. M., & Wallerstein, G. 2005, MNRAS, 356, 963
Yeung, M. C. H., Ponti, G., Freyberg, M. J., et al. 2024, A&A, 690, A399
Zhu, E., & Preibisch, T. 2025, A&A, 694, A93

Appendix A: The impact of optical loading on the spectrum of bright stars

When an X–ray photon reaches the depletion layer of an X–ray CCD, it creates electron–hole pairs there (Dennerl et al. 2020; Meidinger et al. 2021). The same may happen when an optical photon reaches this layer. In contrast to an X–ray photon, however, where the number of released electrons can be utilized for spectroscopy, the absorption of a single optical photon releases typically only one electron. This charge alone is not high enough to get included into the telemetry stream, because it is below the low energy threshold, which needs to be applied in order to prevent telemetry overload due to electronic noise. In the case of celestial sources which are both optically and X–ray bright, however, the similar (though not identical) optical and X-ray point-spread function (PSF) favour the case that the charge clouds created by the optical and X-ray photons get superimposed within the integration time of a particular CCD frame. In the following we discuss the consequences of that case.

For better clarity we start with a simplified example, which considers the presence of only one X-ray and one optical photon and assumes absence of electronic noise. In that case, the observed spectrum is modified due to the additional charge generated by the optical photon in two ways:

- energy: the spectrum gets 'blue-shifted', and because of the Poissonian nature of the additional charge, it gets (somewhat) smeared; while these effects are most apparent at low energies, they affect the whole spectrum.
- flux: the geometry and extent of the charge cloud get modified, causing a change of the reconstructed flux.

While the consequences of optical loading on the energy is straightforward, its impact on the flux requires a more detailed investigation. We need to consider that the charge cloud created by an X–ray photon may extend over up to four pixels, which we refer to as `'singles (s)'`, `'doubles (d)'`, `'triples (t)'`, and `'quadruples (q)'`. The `triples` and `quadruples` have to meet the following criteria in order to have been generated by an X–ray photon: the `triples` must be L-shaped, with the main pixel (the one containing the dominant charge component) at the corner, and the quadruples must be quadratic, with the main pixel essentially opposite to the pixel containing the minimum charge. Only such `triples` and `quadruples` are considered as 'valid' and are used for reconstructing the flux (for the `singles` and `doubles` there is no restriction on their validity other than that they must be sufficiently far away from an insensitive area). The additional charge generated by an optical photon can then modify the pixel pattern in several ways:

1. it neither changes the pattern size nor the validity of the pattern: then only the energy is affected, but not the flux (when taking the energy shift into account); this holds also for the pattern-specific flux, derived, e.g., from considering only singles.
2. it increases the pattern size, but keeps the pattern valid: then the energy and the pattern-specific flux are affected, but not the 'sdtq' flux; the increase of the pattern size is caused by raising the charge in a neighbouring pixel above the low energy threshold.
3. it makes the pattern invalid: then the X–ray photon gets lost and the flux is reduced, but the energy scale is not affected.

If we consider the presence of several optical photons (optical pile-up), then this situation stays unaffected as long as the optical photon flux is not high enough to generate charge above the low energy threshold without an X–ray photon. However, when this happens, the affected pixels have to be masked out in order to avoid saturation of telemetry. Therefore, this case does not need further consideration. Similarly, the presence of several X–ray photons (X–ray pile-up) as well as the combination of optical and X–ray pile–up does not need to be considered here, because it might prevent a spectroscopic analysis.

What still needs to be considered is the presence of electronic noise, which is steeply rising towards the low energy threshold (which is the reason why such a threshold needs to be applied). Superposition with the charge released by optical photons causes its spectrum to get 'blue–shifted' in a similar way as an X–ray spectrum, making it appear amplified and creating the impression of the presence of an additional soft 'optical' component. While to some extent this effect is mitigated by considering the local background in the spectral analysis, an apparent soft energy component may remain. For completeness we mention that there is in addition particle induced background present, which may also be affected by optical loading. This component, however, is comparatively faint.

Appendix A.1: Between patterns and TMs

The effects described above can be utilized for studying the eROSITA spectra for evidence of optical loading. In the following we present FGK spectra which are divided by the effective area (indicated by 'cm^{-2}') for better clarity as significant number of FGK stars are optically bright, with G-band magnitudes below 5, potentially causing strong optical loading.

Figure A.1a investigates the effect 1 by comparing pattern-specific spectra: `'s'` (black) with `'dtq'` (red). The fact that `'s'` is only slightly below `'dtq'` indicates that the pattern size and validity of the patterns are not much affected, indicating only minor optical loading. In contrast, Figure A.1b presents a case where `'s'` is considerably below `'dtq'`, which is evidence for substantial optical loading. Subdividing the `'dtq'` spectrum of Figure A.1b into the individual `'d'`, `'t'`, and `'q'` components (Figure A.1c) shows that the apparent spectral flux increases with pattern size up to triples. This is consistent with effect 2: if the charge cloud created by the absorption of an X–ray photon is distributed over more pixels, then the probability that an optical photon hits a pixel in that cloud is increased. This, however, does not apply to quadruples, because any extension beyond four pixels makes a pattern invalid, leading to a loss of flux (effect 3). This loss, however, is quite small, because the probability that quadruples are created by an X–ray photon below 0.5 keV is less than 3%.

Another way of checking for optical loading is to compare the spectra between `TM8` and `TM9`, as they differ in the thickness of the Al layer in the optical blocking filter, which is 200 nm for `TM8` and 100 nm for `TM9` (Meidinger et al. 2021). Thus, `TM9` is more sensitive to optical flux than `TM8`. Figure A.1d shows that for source #13 (the same as in Figure A.1a) the `'sdtq'` spectra for `TM8` and `TM9` (when divided by the effective area) are similar. This indicates that the derived luminosity is not much affected by optical loading (effect 2), consistent with the conclusion above, which was based on a comparison between the `'s'` and `'dtq'` spectra for `TM8` (effect 1, Figure A.1a). For source #34 (Figure A.1e), however, `TM9` is clearly below `TM8`, and for source #38 (Figure A.1f), `TM9` is considerably below `TM8` a clear indication for optical loading. Source #13, #34 and #38 are eps Eri (K2V star with G3.5 mag), π^3 Ori (F6V star with G3.2 mag), and β Hy (G0V subgiant with G2.7 mag). We conclude that for FGK stars fainter than ∼3.5 mag, our broad–band flux values are essentially unaffected by optical loading.

Appendix A.2: Optically bright and faint M stars

In Section 6, we conclude the best-fit modeling of average M stars is 3T-APEC, though the softest component is with strangely low temperature (0.04 keV) and unconstrained normalization. Although optical loading was suspected initially for this soft component, all M dwarfs are fainter than the suggested optical loading threshold G = 5. The only two cases with companion stars brighter than G5 mag were removed from the sample.

Here we divide the M-dwarf sample into optically-bright and optically-faint groups using more conservative G-band magnitude cuts (G = 10). The counts spectra of two groups are presented in Figure A.2, in the middle panels shows the ratio between optically-bright and -faint. All spectra are binned with minimal 20 counts in each channel. To facilitate the comparison, the spectrum of the M-Gfaint sample has been scaled up by a factor of 1.9 to match the flux level of the optically-bright M subset at 0.7 keV. The ratio shows not soft excess for optically-bright groups and the two spectra are remarkable similar cross the band. We therefore conclude that the M-dwarf sample is not affected by optical loading. Instead, it likely originates from genuine emission that might be associated with deep coronal layers or cool regions.

Appendix A.3: Optically bright and faint FGK stars

To investigate the impact of optical loading, in Figure A.2 we compare the stacked spectra of the 22 optically-bright FGK sample (green: G<5) with that of a subset of 9 less optically bright FGK stars (violet: G>5). For display it is scaled up by 4.3 times to match the optically-bright FGK subset at 0.7 keV (ratio normalized to 1 at 0.7 keV).

The ratio in the bottom panel of Figure A.2 between the two spectra already reveals noticeable differences: below 0.35 keV, the G-bright spectrum shows a strong excess with a ratio exceeding 2. We show as well the energy up to 2.5 keV for comparing. In addition, a slight mismatch around the emission lines above 1 keV may be related to the energy-shift effect of optical loading (as discussed in Effect 1 above).

We fit both spectra the 3T-APEC model in 0.2–2.5 keV. In Table A.1, we list the best-fit parameters: The fitted parameters for the optically bright and optically faint FGK stars are not consistent. The optically bright FGK group shows temperature and abundance values that are consistent with those of the full FGK sample, whereas the optically faint FGK group yields different temperature components. Moreover, a very soft component is required to fit the optically bright FGK spectra but is not required in the optically faint group (unconstrained normalization). This suggests that the optically bright FGK stars may dominate the average (all) FGK spectral shape and, ideally, should be excluded when aiming to isolate the impact of optical loading. However, the 10-pc optically faint FGK subset comprises only nine stars and therefore provides insufficient statistics. For such a small sample, fitting a three-temperature APEC model is likely to be driven by intrinsic source-to-source differences rather than by the effect of optical loading. This limitation highlights the need for a larger volume-limited sample in future work.

Appendix A.4: Test of removing central optical 'pile-up'

To evaluate the impact of optical loading near the PSF core, we performed a test by excluding the central 5″ region of all FGK and M dwarf sources prior to stacking their spectra. This method aims to reduce potential optical pile-up or loading effects concentrated in the image centre.

Figures A.3 and A.4 show a comparison between the original stacked spectra and those obtained after central-region removal, for FGK stars and M dwarfs, respectively.

For the FGK stars, we observe a ∼20% decrease in flux within the soft X-ray band (0.2–0.35 keV), while no significant (lower than 3%) changes are seen at higher energies. Combined with the pattern-based tests indicating the presence of optical loading, this result suggests that the FGK sample is primarily affected in the soft band. In contrast, the M dwarf spectra is lowed by 25% across the full energy range.

Table A.1: Fitting parameters for optically bright and faint FGK stars.

Param.	All FGK	Opt-bright FGK G<5	Opt-faint FGK G>5
kT_1	0.072 ± 0.003	0.071 ± 0.003	0.07 fixed
N_1	33^{+11}_{-9}	56^{+16}_{-14}	1^{+3}_{-1}
kT_2	0.36 ± 0.02	0.37 ± 0.02	0.20 ± 0.03
N_2	3.9 ± 0.8	6 ± 1	3 ± 1
kT_3	0.80 ± 0.03	0.80 ± 0.03	0.60 ± 0.07
N_3	2.4 ± 0.6	5 ± 1	2 ± 1
Z	$0.7^{+0.2}_{-0.1}$	0.6 ± 0.1	$0.4^{+0.4}_{-0.2}$
$\chi^2_\nu \frac{\chi^2}{d.o.f.}$	$1.4 \frac{432.3}{301}$	$1.3 \frac{272.32}{207}$	$0.6 \frac{79.76}{129}$

Notes. The 3T-APEC model is used to fit in energy range 0.2–2.5 keV. Except for the all FGK spectrum, the channel is binned to have minimal 20 counts. $N_{\rm apec}$ is in the unit $10^{-4} \frac{10^{-14}}{4\pi(10{\rm pc})^2}$ cm^{-5}.

Appendix B: Impact of different stacking method

Table B.1: Best-fit parameters for M stars using different stacking strategies.

Param.	AC	AC T_lt_3000	AR	AR T_lt_3000
kT_1	0.27 ± 0.01	0.27 ± 0.01	0.269 ± 0.008	0.268 ± 0.008
N_1	1.7 ± 0.2	1.8 ± 0.2	1.5 ± 0.1	1.5 ± 0.1
kT_2	0.94 ± 0.03	0.95 ± 0.03	0.97 ± 0.03	0.97 ± 0.02
N_2	1.1 ± 0.1	$1.3^{+0.1}_{-0.2}$	1.00 ± 0.09	1.0 ± 0.1
Z	0.28 ± 0.04	0.27 ± 0.04	0.32 ± 0.04	0.32 ± 0.04
χ^2_ν ($\frac{\chi^2}{\rm d.o.f.}$)	$0.93 \frac{231.50}{249}$	$0.70 \frac{172.63}{249}$	$2.2 \frac{550.61}{249}$	$2.2 \frac{559.26}{249}$
$L_{0.2\text{-}2.0}$	2.6 ± 0.1	2.89 ± 0.06	2.53 ± 0.04	2.58 ± 0.04

Notes. AC (Averaging Counts), AC_T_lt_3000 (excluding sources with exposure > 3000 s), AR (Averaging Rates) and AC T_lt_3000 (excluding sources with exposure > 3000 s). $N_{\rm apec}$ is in the unit $10^{-4} \frac{10^{-14}}{4\pi(10{\rm pc})^2}$ cm^{-5}. Luminosities is in 0.2–2.0 keV with units of 10^{27} erg s^{-1} .

Table B.1 and Table B.2 compare the spectral fitting results of the 3T-APEC model obtained using different stacking methods for M and FGK stars. Additionally, we also generated a version of the average spectrum excluding highly exposed sources (for M star is those with exposure times exceeding 3000 seconds, for FGK is 1400 seconds), referred to as T_lt_xxxx for both Averaging Counts (AC) method and Averaging Rates (AR) method.

The AR methods yield significantly larger reduced chi-squared values compared to those from the AC method. This is expected, as the error bars in the AR method are likely underestimated due to the assumption of Gaussian noise rather than

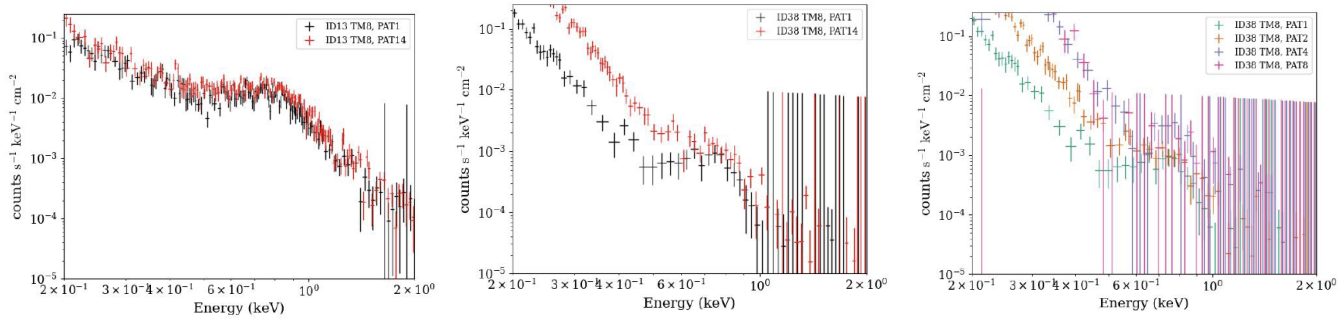

(a) TM8 spectra for source #13: 's' (black) and 'dtq' (red).

(b) TM8 spectra for source #38: 's' (black) and 'dtq' (red).

(c) TM8 spectra for source #38: 's' (green), 'd' (blue), 't' (purple), and 'q' (red).

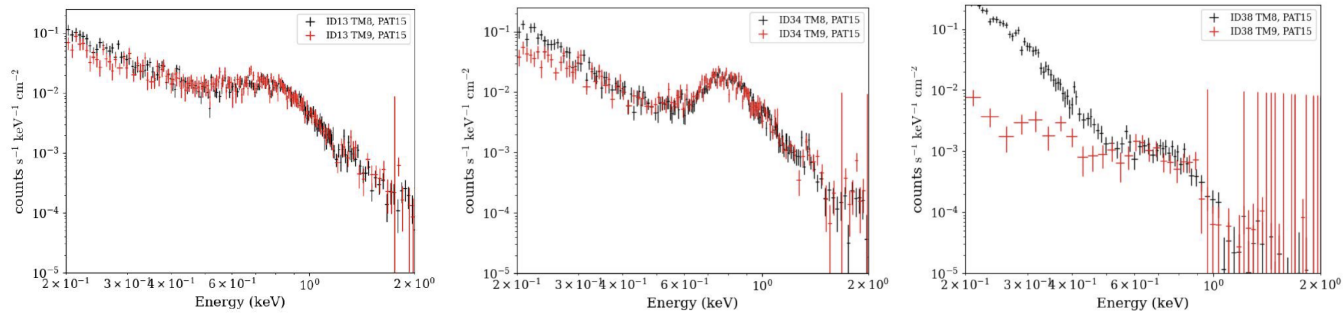

(d) 'sdtq' spectra for source #13: TM8 (black) and TM9 (red).

(e) 'sdtq' spectra for source #34: TM8 (black) and TM9 (red).

(f) 'sdtq' spectra for source #38: TM8 (black) and TM9 (red).

Fig. A.1: Event-pattern and -TM selection effects for three optically bright stars: eps Eri (#13, K2V star with G3.5 mag), π^3 Ori (#34; F6V star with G3.2 mag), and β Hy (#38; G0V subgiant with G2.7 mag).

Table B.2: Best-fit parameters for FGK stars using different stacking strategies.

Param.	AC	AC T_lt_1400	AR	AR T_lt_1400
kT_1	0.09 ± 0.01	0.101 ± 0.009	0.097 ± 0.007	0.102 ± 0.008
N_1	10^{+5}_{-3}	7^{+3}_{-2}	9^{+3}_{-2}	7 ± 2
kT_2	0.35 ± 0.02	0.36 ± 0.02	0.35 ± 0.01	0.35 ± 0.01
N_2	4.6 ± 0.8	5.1 ± 0.9	5.5 ± 0.9	6 ± 1
kT_3	0.79 ± 0.03	0.79 ± 0.03	0.81 ± 0.03	0.81 ± 0.02
N_3	3.1 ± 0.6	3.5 ± 0.7	3.4 ± 0.6	3.5 ± 0.7
Z	$0.55^{+0.13}_{-0.09}$	$0.54^{+0.13}_{-0.09}$	0.6 ± 0.1	0.6 ± 0.1
χ^2_ν ($\frac{\chi^2}{\text{d.o.f.}}$)	$1.15 \frac{252.77}{219}$	$1.18 \frac{257.44}{219}$	$2.10 \frac{460.83}{219}$	$2.16 \frac{472.60}{219}$
$L_{0.35\text{-}2.0}$	12.1 ± 0.2	13.0 ± 0.2	14 ± 1	15.3 ± 0.5

Notes. AC (Averaging Counts), AC_T_lt_1400 (excluding sources with exposure > 3000 s), A (Averaging Rates) and AC T_lt_1400 (excluding sources with exposure > 1400 s). Luminosities is in 0.35–2.0 keV with units of 10^{27} erg s^{-1} .

Poisson statistics. Across all approaches, the best-fit temperatures and metallicities remain broadly consistent, indicating robustness in the overall spectral shape. The total luminosities obtained using the AC and AR methods are 2.6×10^{27} and 2.53×10^{27} erg s^{-1} for M stars, and 12.1×10^{27} and 14×10^{27} erg s^{-1} for FGK stars. The discrepancy is only seen for the FGK sample. We interpret it as a systematic effect arising from the choice of stacking procedure, likely amplified by intrinsic star-to-star differences within the sample, as discussed in Section 4. When comparing luminosities, we find that excluding the highly exposed sources in the AC method does not significantly alter the spectral shape but increases the total luminosity by approximately 10% in the 0.2–2.0 keV band for M stars and 8% for FGK stars.

Appendix C: Spectrum extraction for individual sources

The extraction of source and background was carried out with `srctool` (Brunner et al. 2022), with source and background radius adaptively chosen for detected source (`exttype=AUTO`) and fixed radius (source radius: 45", background annulus radius: 60", 99") for the undetected sources (`exttype=POINT`). The fixed 45" sources radius is about 3 time of the `HEW` of SRG/*eROSITA* survey mode. For the detected sources, the automatically determined source and background radii take into account the PSF, the detected counts, the background level, and the detection likelihood. A few customized settings for the AUTO mode of `srctool` we used are listed in Table C.1 [2].

Amongst these settings, the most important is `SRCTOOL_AUTOREG_BACK_TO_SRC_AREA_RATIO`, which defines the background region to be three times larger than the source region. The detection status of the stars was determined by cross-matching with the `eRASS:1` catalogue (Merloni et al. 2024), selecting the nearest source within 15″, followed by visual inspection. In cases where additional X-ray sources were present within the extraction region, they were masked using circular regions with radii equal to twice the `APERTURE` radius from the catalogue to minimize contamination from nearby sources.

[2] See: https://erosita.mpe.mpg.de/edr/DataAnalysis/srctool_doc.html

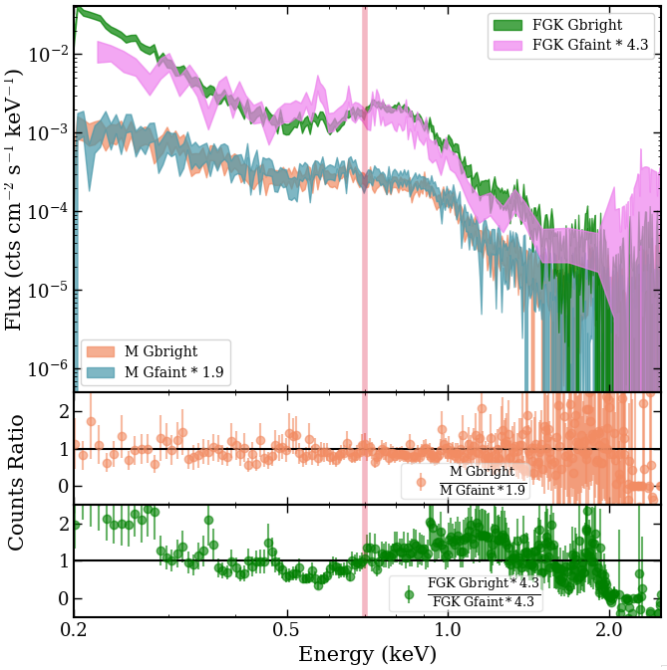

Fig. A.2: X-ray stacked spectra for the optically-bright M dwarf stars (orange: $m_G < 10$), optically-faint (blue: $m_G > 10$) M dwarf stars, optically-bright FGK dwarf stars (green: $m_G < 5$) and optically-faint (violet: $m_G > 5$) FGK dwarf stars. The middle and bottom panels display the ratio between the two groups of spectra.

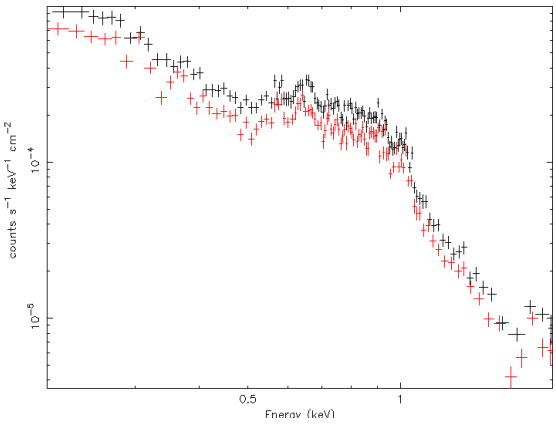

Fig. A.3: Comparison between the original M stacked spectrum (black) and that obtained after excluding the central 5″ region from each source (red).

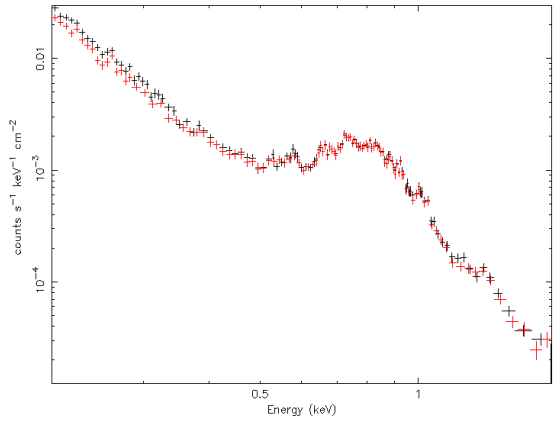

Fig. A.4: Comparison between the original FGK stacked spectrum (black) and that obtained after excluding the central 5″ region from each source (red).

Table C.1: SRCTOOL autoregistration parameters.

Parameter	Value
SRCTOOL_AUTOREG_MINIMUM_SOURCE_RADIUS	45
SRCTOOL_AUTOREG_INITIAL_SRC_R_TO_BACK_R1	1.2
SRCTOOL_AUTOREG_MAX_SRC_MAP_TO_BG_MAP_RATIO	0.2
SRCTOOL_AUTOREG_BACK_TO_SRC_AREA_RATIO	3.0
SRCTOOL_AUTOREG_MAX_CONF_MAP_TO_SRC_MAP_RATIO	0.1
SRCTOOL_AUTOREG_MAX_RATIO_BAC_R1_TO_RADIUS_99PC	1
SRCTOOL_AUTOREG_MAX_BACK_ANNULUS_WIDTH	120

Table D.1: Fits of M dwarf with 1T-VAPEC using different initializations for the metal abundances.

Param.	Model A	Model B	Model C
kT1	$0.45^{+0.03}_{-0.02}$	0.46 ± 0.02	0.46 ± 0.02
N1	3.0 ± 0.3	3.6 ± 0.2	4.9 ± 0.3
A_He	=1	=1	0.10 ± 0.04
A_Rest	=A_Ne	=A_C	=A_He
A_C	=A_Ne	0.12 ± 0.05	=A_He
A_O	0.23 ± 0.05	0.19 ± 0.04	$0.12^{+0.04}_{-0.03}$
A_Ne	0.5 ± 0.1	0.63 ± 0.06	0.47 ± 0.03
A_Si	0.6 ± 0.02	0.38 ± 0.2	0.3 ± 0.1
A_Fe	0.09 ± 0.02	0.06 ± 0.01	0.041 ± 0.008
χ^2(d.o.f.)	$1.75 \frac{433.75}{248}$	$1.01 \frac{249.48}{247}$	$1.03 \frac{255.33}{247}$

Notes. The fitted energy range is 0.2–2.0 keV. 90% uncertainty is reported. $N_{\rm apec}$ is in the unit $10^{-4} \frac{10^{-14}}{4\pi(10{\rm pc})^2}$ cm^{-5}. The model C is the one used in Table 2.

Appendix D: More configuration of elemental abundance for VAPEC

Here we show the result from fitting M dwarf stars with 1T-VAPEC and 2T-VAPEC (Table D.1 and D.2 respectively) using different initializations for the metal abundances. Parameters fixed to a number or to another parameter are shown by the = symbol. We adopt model C in the main text because it provides good fits for both the M- and FGK-star samples without imposing an arbitrary fixed He abundance or yielding unphysical parameter values. We note, however, that alternative model configurations may also be plausible.

Appendix E: bootstrap resampling

Besides the fit uncertainty, we perform a bootstrap resampling to estimate the uncertainty on the fit values by computing their scatter across the different realizations. This is a repeatable resampling from the full stars that form the same volume. In practice, we do 1000 realization. After stacking and fitting again every realization, we derive systematic uncertainties on each parameter by [5%, 95%] confidence intervals (90% CI) from the obtained distribution of their values. The corresponding values are reported in the fit summary tables presented as Table 2 for M stars and Table 6 for FGK stars.

Table D.2: Fits of FGK dwarf with 2T-VAPEC using different initializations for the metal abundances.

Param.	Model O	Model A	Model B	Model C
kT1	$0.26^{+0.02}_{-0.03}$	$0.26^{+0.2}_{-0.3}$	$0.22^{+0.02}_{-0.01}$	0.22 ± 0.01
N1	10.2 ± 4	8 ± 3	8 ± 1	10 ± 2
KT2	0.74 ± 0.06	0.74 ± 0.06	0.60 ± 0.02	0.60 ± 0.02
N2	6 ± 1	5 ± 0.9	7 ± 1	8 ± 2
A_He	=A_Ne	=1	=1	$0.3^{+0.2}_{-0.1}$
A_Rest	=A_Ne	=A_Ne	=A_C	=A_He
A_C	=A_Ne	=A_Ne	$0.40^{+0.18}_{-0.12}$	=A_He
A_O	$0.18^{+0.14}_{-0.05}$	$0.23^{+0.12}_{-0.06}$	$0.18^{+0.07}_{-0.05}$	$0.14^{+0.06}_{-0.04}$
A_Ne	$0.4^{+0.4}_{-0.2}$	$0.5^{+0.4}_{-0.2}$	1.0 ± 0.3	$0.8^{+0.3}_{-0.2}$
A_Si	$0.17^{+0.13}_{-0.09}$	0.2 ± 0.1	0.2 ± 0.1	$0.18^{+0.12}_{-0.09}$
A_Fe	$0.35^{+0.11}_{-0.07}$	$0.44^{+0.13}_{-0.07}$	$0.35^{+0.09}_{-0.06}$	$0.27^{+0.09}_{-0.06}$
χ^2(d.o.f.)	$1.17\ \frac{264.25}{218}$	$1.21\ \frac{264.53}{218}$	$1.09\ \frac{235.81}{217}$	$1.08\ \frac{235.16}{217}$

Notes. The fitted energy range is 0.35–2.0 keV. The model C here is the one used in Table 6.

Appendix F: Luminosity in single eRASS

Figure F.1 shows the variation in the average X-ray luminosity of nearby M (top) and FGK (bottom) dwarfs across the four eROSITA all-sky surveys (eRASS1 to eRASS4). The overall consistency indicates that the mean luminosities derived for the 10-pc M- and FGK-dwarf samples defined in WGH are stable over time and not significantly affected by temporal variability.

Appendix G: Assessing log-normal DEM models for M and FGK spectra

We test to fit the average spectra with a multi-temperature plasma model that represents the emission as a log-normal distribution of APEC components, namely lognorm[3]. It approximates the differential emission measure by summing N discrete temperature components (default N=21) with temperatures evenly spaced in $\ln T$. Each component is weighted by $w_i \propto \exp\left[-\frac{1}{2}\left(\frac{\ln T_i - \ln T_c}{\ln \sigma}\right)^2\right]$. As the width parameter decreases, the distribution approaches a single-temperature `apec` model. In Table G.1, we show that the single-`lognorm` fits improve upon the 1T-APEC and 1T-VAPEC models, but the overall fit quality remains poor. While the two-`lognorm` model provides acceptable fits for both stellar groups, it does not outperform the 2T-APEC model and yields poorly constrained width parameters (logsigma). We therefore find no statistically compelling evidence that `lognorm` models are required to describe the spectra.

A further insight from the single-`lognorm` fits is that they help explain the unrealistically low abundances obtained in the 1T case. For the M-star spectrum, the 1T-APEC fit yields Z=0.061, well below the ~0.1–1$Z_\odot$ found in optical and infrared studies of local M dwarfs (Montes et al. 2018; Neves et al. 2012; Woolf & Wallerstein 2005). This experiment with lognorm supports the interpretation that the extremely low metallicity is an artefact of modelling an intrinsically multi-temperature spectrum with an oversimplified 1T model.

Appendix H: Table of all stars

Table H.1 and Table H.2 list the full set of stars included in our analysis and initially identified and catalogued by Caramazza et al. (2023). For each object, the table provides the identifier, coordinates (RA and DEC) at J2020, distance in parsecs, spectral type, *Gaia* G-band magnitude, and a flag indicating whether the source is detected in the `eRASS1 catalogue` (denoted as `IF_ERASS`. The final column gives additional comments, including cross-matches with commonly known catalogue names. Distance in pc are computed as 1000/PARALLAX (mas), where the parallax values are taken from *Gaia* EDR3 (Reylé et al. 2021). Their 10 pc sample also includes stars slightly beyond 10 pc (e.g. 10.2 pc), whose parallax uncertainties make them statistically consistent with being within 10 pc.

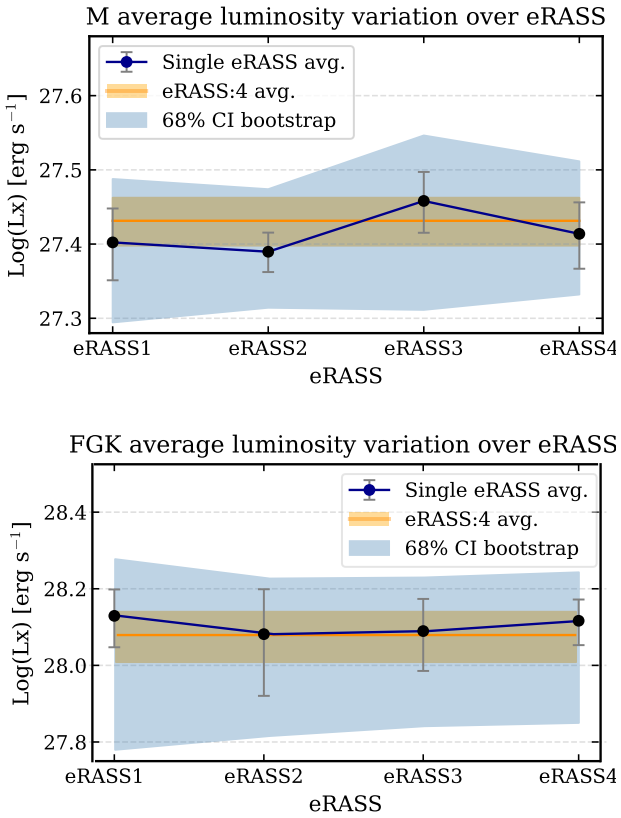

Fig. F.1: Average X-ray luminosity variation of nearby M (top) and FGK (bottom) dwarfs over the four eROSITA all-sky surveys (eRASS1 to eRASS4). Blue points represent the average luminosity from individual eRASS epochs, with vertical bars indicating the methodological uncertainties. The orange horizontal band shows the average luminosity obtained from the combined eRASS:4 spectra, while the shaded blue area indicates the 68% confidence interval estimated via bootstrap resampling.

Table G.1: Fits using model `lognorm`.

Param.	M-1lognorm	M2lognorm	FGK -1lognorm	FGK-2lognorm
kT1	$0.41^{+0.02}_{-0.06}$	0.26 ± 0.01	$0.44^{+0.02}_{-0.02}$	0.29 ± 0.03
logsigma	$0.9^{+0.2}_{-0.1}$	$0.08^{+0.07}_{-0.08}$	0.55 ± 0.06	$0.14^{+0.07}_{-0.14}$
Z	$0.24^{+0.03}_{-0.05}$	$0.29^{+0.06}_{-0.05}$	$0.37^{+0.09}_{-0.06}$	0.34 ± 0.06
N1	3.1 ± 0.3	1.1 ± 0.1	12 ± 1	7 ± 1
kT2		0.94 ± 0.03		$0.71^{+0.06}_{-0.05}$
N2		1.6 ± 0.2		$6.0^{+0.6}_{-1.0}$
χ^2(d.o.f.)	$1.6\ \frac{405.45}{250}$	$0.93\ \frac{230.70}{248}$	$1.81\ \frac{403.13}{222}$	$1.58\ \frac{346.90}{220}$

[3] See: https://github.com/jeremysanders/lognorm

Table H.1: *Gaia* 10 pc M stars. Rate_e1 denotes the eRASS1 catalogue count rate (Merloni et al. 2024), taken from the column `ML_RATE_0_e1`, i.e., the 0.2–2.3 keV band rate. [a]: Flag A - field crowded; Flag B - optical loading; Flag C- close pair. Detailed definition see Section 2.

ID	OBJ_NAME	RA_mean	DEC_mean	D (pc)	SpT	G (mag)	eRASS1 Catlog.	Gliese Name	Comm.[a]	Rate_e1
5	L 35-12	139.289739	-77.827856	9.521 ± 0.002	M4.5V	11.5566	TRUE	GJ 1123		0.05 ± 0.01
8	L 471-42	189.699638	-38.389215	6.663 ± 0.001	M4.5V	11.2262	TRUE	GJ 3737		0.06 ± 0.02
10	L 143-23	161.084287	-61.200422	4.832 ± 0.001	M5.5V	11.8594	FALSE	GJ 3618		-
17	AD Leonis	154.898084	19.869750	4.965 ± 0.001	M3V	8.2040	TRUE	GJ 388		25.50 ± 0.60
18	GJ 832	323.391156	-49.013754	4.967 ± 0.001	M2V	7.7399	TRUE	GJ 832		0.14 ± 0.05
20	L 49-19	343.915846	-75.464834	8.597 ± 0.001	M3V	9.2927	TRUE	GJ 877		0.13 ± 0.03
21	UCAC4 195-119117	235.199442	-51.028548	5.327 ± 0.001	M6V	12.7359	TRUE			0.07 ± 0.02
23	GJ 176	70.736437	18.951667	9.485 ± 0.002	M2V	9.0044	TRUE	GJ 176		0.06 ± 0.02
28	HD 191849	303.478909	-45.164951	6.165 ± 0.001	M0.5V	7.2426	TRUE	GJ 784		0.25 ± 0.06
32	GJ 581	229.854606	-7.722841	6.300 ± 0.001	M3V	9.4217	FALSE	GJ 581		-
33	CD-51 6859	189.457785	-52.001305	9.492 ± 0.002	M3V	9.5650	TRUE	GJ 479		0.88 ± 0.07
35	GJ 570 B	224.366845	-21.421181	5.9 ± 0.8	M1.5V	7.2492	TRUE	GJ 570 A	Flag A	1.19 ± 0.09
42	G 42-24	148.477730	20.948620	9.545 ± 0.003	M4.5V	12.3635	TRUE	GJ 3571		0.20 ± 0.05
45	HD 50281 Ba	103.071805	-5.190088	8.750 ± 0.002	M2.5V	9.0975	TRUE	Flag A		0.21 ± 0.06
47	CD-45 5378	146.120459	-45.779899	9.419 ± 0.001	M2.5V	9.1587	TRUE	GJ 367		0.06 ± 0.02
49	WT 460 A	212.994105	-41.539815	9.11 ± 0.02	M5.5V	13.4190	TRUE			0.21 ± 0.04
51	GJ 667 C	259.753153	-34.998092	7.243 ± 0.001	M2V	9.3861	FALSE		Flag A	-
65	Wolf 358	162.711778	6.803363	6.967 ± 0.001	M4V	10.2907	FALSE	GJ 402		-
66	BD-18 359 A	31.278116	-17.615637	9.32 ± 0.02	M2.5V	9.1705	TRUE	GJ 84 A		0.10 ± 0.03
68	GJ 486	191.979981	9.748721	8.079 ± 0.002	M3.5V	10.1051	FALSE	GJ 486		-
69	CD-68 47 A	17.601313	-67.441587	7.88 ± 0.02	M3V	8.7420	TRUE	GJ 54 A		0.12 ± 0.03
71	L 674-15	123.170455	-21.555979	8.117 ± 0.002	M4V	10.6716	FALSE	GJ 300		-
73	G 13-22	183.563417	0.622336	8.088 ± 0.003	M5V	11.8286	TRUE	GJ 1154		0.55 ± 0.07
74	HD 95735	165.829974	35.942082	2.546 ± 0.000	M2V	6.5511	TRUE	GJ 411		1.04 ± 0.11
75	Kapteyn's Star	77.972578	-45.051665	3.934 ± 0.000	M0.5V	8.0635	TRUE	GJ 191		0.04 ± 0.01
76	Ross 64	96.175515	23.430079	8.494 ± 0.002	M4V	11.6625	FALSE	GJ 232		-
77	GJ 1061	54.004832	-44.514876	3.674 ± 0.000	M5.5V	10.9954	TRUE	GJ 1061		0.05 ± 0.01
78	BD+01 2447	157.227954	0.836740	7.038 ± 0.001	M2V	8.6759	TRUE	GJ 393		0.15 ± 0.05
79	Ross 837	209.556042	12.583054	9.360 ± 0.004	M3.5V	11.0511	TRUE	GJ 3817		0.04 ± 0.02
80	AN Sex	153.072727	-3.747083	7.707 ± 0.001	M2V	8.3317	TRUE	GJ 382		0.54 ± 0.08
81	Proxima Cen	217.380988	-62.675016	1.302 ± 0.000	M5.5V	8.9847	TRUE	GJ 551		3.61 ± 0.16
86	G 109-35	104.875677	19.343643	7.753 ± 0.004	M5.5V	12.7764	FALSE	GJ 1093		-
89	Wolf 424 B	188.312294	9.022109	4.475 ± 0.009	M5V	11.2401	TRUE	GJ 473 B	FLAG C	2.21 ± 0.15
91	SCR J1138-7721	174.514990	-77.359910	8.379 ± 0.002	M5.5V	12.8162	FALSE			-
95	PM J11413-3624	175.343179	-36.407786	8.689 ± 0.003	M4V	11.5837	FALSE			-
96	LP 991-84	24.841623	-39.603823	8.726 ± 0.003	M5V	12.5683	FALSE			-
97	Ross 47	85.550522	12.480201	5.791 ± 0.001	M4V	10.1137	FALSE	GJ 213		-
99	CD-40 5404	144.939134	-41.065479	9.607 ± 0.002	M3V	9.6314	TRUE	GJ 358		1.34 ± 0.12
107	SCR J0740-4257	115.045352	-42.958254	7.981 ± 0.001	M5V	12.0307	TRUE			0.67 ± 0.07
108	Ross 695	186.225477	-18.255733	8.875 ± 0.002	M2.5V	10.2900	FALSE	GJ 465		-
110	G 100-28 A	85.107758	24.800031	10.2 ± 0.3	M5.5V	13.3290	TRUE	GJ 1083 A		0.37 ± 0.07
117	LP 776-46	75.832293	-17.376122	9.236 ± 0.003	M3V	10.5616	FALSE	GJ 3325		-
119	G 112-50	117.979331	-0.007810	9.272 ± 0.004	M4.5V	11.6534	FALSE	GJ 1103 A		-
120	HD 32450 A	75.617585	-21.258249	8.363 ± 0.003	M0.5V	7.7924	TRUE	GJ 185 A	FLAG C	0.12 ± 0.03
122	G 41-14 B	134.736998	8.472024	6.77 ± 0.09	M4V	10.3290	TRUE	GJ 3522 B	FLAG C	6.71 ± 0.29
124	BD-17 588 A	45.461893	-16.594901	6.864 ± 0.001	M3V	10.0584	TRUE	GJ 3193	FLAG C	1.67 ± 0.10
125	GJ 357	144.007690	-21.666563	9.436 ± 0.002	M2.5V	9.8916	FALSE	GJ 357		-
130	GJ 251	103.698934	33.265860	5.585 ± 0.001	M3V	8.8635	TRUE	GJ 251		0.10 ± 0.04
131	L 347-14	290.205411	-45.575090	5.909 ± 0.002	M4V	10.7529	FALSE	GJ 754		-
132	41 Ara B	259.770440	-46.636169	8.83 ± 0.03	M0.5V	7.9870	FALSE	GJ 666 B		-
133	Ross 619	122.996172	8.743393	6.769 ± 0.004	M4V	11.3972	FALSE	GJ 299		-
134	L 173-19	30.160714	-55.968356	8.216 ± 0.002	M3.5V	10.5571	TRUE			0.06 ± 0.02
135	G 113-20	124.031065	1.302926	8.939 ± 0.002	M2V	9.1331	FALSE	GJ 2066		-
136	BD-17 588 B	45.461893	-16.594901	6.864 ± 0.001	M3.5V	10.4310	TRUE	GJ 3193 B	FLAG C	1.67 ± 0.10
137	HD 102365 B	176.624462	-40.494333	8.028 ± 0.003	M4V	11.7247	TRUE	GJ 442 B	FLAG B	0.03 ± 0.01
138	CD-44 3045 A	104.435181	-44.291463	9.309 ± 0.003	M3V	10.4182	TRUE	GJ 257 A	FLAG C	0.04 ± 0.02
139	CD-40 9712	233.044774	-41.281592	5.917 ± 0.001	M2.5V	8.2741	TRUE	GJ 588		0.28 ± 0.06
140	G 41-14 A	134.736866	8.472006	6.77 ± 0.09	M4V	9.97131	TRUE	GJ 3522 A	FLAG C	6.71 ± 0.29
141	HD 260655	99.290328	17.566781	9.998 ± 0.002	M0.5V	8.8782	TRUE	GJ 239		0.07 ± 0.03
142	GJ 273	111.855418	5.204304	3.786 ± 0.001	M3.5V	8.5763	TRUE	GJ 273		0.11 ± 0.04
143	Ross 128	176.938524	0.797437	3.375 ± 0.000	M4V	9.6010	TRUE	GJ 447		0.20 ± 0.05
144	G 9-38 A	134.558068	19.762822	5.151 ± 0.003	M5.5V	11.9662	TRUE	GJ 1116 A	FLAG C	0.94 ± 0.12
145	G 161-7 A	138.899291	-10.597554	9.68 ± 0.09	M5V	12.0050	TRUE			0.46 ± 0.07
146	Wolf 424 A	188.311992	9.022391	4.327 ± 0.010	M5.5V	11.2351	TRUE	GJ 473 A	FLAG C	2.21 ± 0.15
147	Ross 104	165.015041	22.831314	6.748 ± 0.001	M2.5V	8.9770	TRUE	GJ 408		0.15 ± 0.05
148	L 403-31	210.961771	-42.699747	9.940 ± 0.003	M4V	11.6951	TRUE			0.98 ± 0.08
149	G 99-49	90.016402	2.706319	5.208 ± 0.001	M4V	9.9013	TRUE	GJ 3379		2.99 ± 0.18
150	L 100-115	145.691871	-68.878432	6.504 ± 0.001	M4.5V	11.1332	TRUE	GJ 1128		0.08 ± 0.01
151	L 32-9	98.423335	-75.628355	8.839 ± 0.001	M3V	9.3847	TRUE		FLAG C	0.19 ± 0.02

Continued on next page

ID	OBJ_NAME	RA_mean	DEC_mean	D (pc)	SpT	G (mag)	eRASS1 Catlog.	Gliese Name	Comm.[a]	Rate_e1
152	L 32-8	98.437148	-75.623442	8.839 ± 0.001	M3.5V	10.2122	TRUE		FLAG C	0.19 ± 0.02
153	Ross 614 A	97.351828	-2.818235	4.12 ± 0.01	M4.5V	9.6300	TRUE	GJ 234 A		5.66 ± 0.34
154	CD-48 11837 B	263.805929	-48.677114	9.690 ± 0.004	M3.5V	11.6138	TRUE		FLAG C	0.12 ± 0.04
155	BD+11 2576	202.505778	10.370912	7.628 ± 0.002	M1V	8.2052	FALSE	GJ 514		-
156	SCR J0630-7643 A	97.692710	-76.716283	8.876 ± 0.007	M5.5V	13.2158	TRUE			0.29 ± 0.02
157	GJ 166 C	63.826537	-7.675594	5.014 ± 0.002	M4V	9.77531	TRUE	GJ 166 C	FLAG B	5.47 ± 0.22
158	GJ 229 A	92.643378	-21.868812	5.761 ± 0.001	M1V	7.3134	TRUE	GJ 229 A		0.36 ± 0.06
159	HD 225213	1.393036	-37.370956	4.346 ± 0.001	M2V	7.6824	TRUE	GJ 1		0.07 ± 0.03
160	CD-37 10765 B	245.008169	-37.523965	8.498 ± 0.008	M5V	12.8980	TRUE	GJ 618 b	FLAG C	0.06 ± 0.02
161	AP Col	91.217468	-34.557941	8.666 ± 0.002	M5V	11.1121	TRUE			1.93 ± 0.12
162	GJ 3323	75.486041	-6.949322	5.375 ± 0.001	M4V	10.6493	TRUE	GJ 3323		0.65 ± 0.07
163	Wolf 359	164.097831	6.999014	2.409 ± 0.000	M6V	11.0383	TRUE	GJ 406		1.65 ± 0.16
164	GL Vir	184.739967	11.127232	6.464 ± 0.002	M5.5V	11.9261	TRUE	GJ 1156		0.60 ± 0.08
165	G 9-38 B	134.557322	19.762531	5.095 ± 0.005	M6V	12.4856	TRUE	GJ 1116 B	FLAG C	0.94 ± 0.12
166	L 737-9 A	77.149104	-18.180199	9.231 ± 0.008	M3.5V	9.0548	TRUE	GJ 190 A		0.07 ± 0.02
167	G 89-32 A	114.106052	7.076866	8.58 ± 0.07	M5V	12.0130	TRUE	GJ 3454		0.92 ± 0.12
168	CD-48 11837 A	263.807391	-48.678131	9.680 ± 0.002	M2V	9.29361	TRUE	GJ 680	FLAG C	0.12 ± 0.04
169	CD-37 10765 A	245.009125	-37.523251	8.513 ± 0.002	M3V	9.49538	TRUE	GJ 618 A	FLAG C	0.06 ± 0.02
170	GJ 674	262.171317	-46.900316	4.553 ± 0.001	M3V	8.3364	TRUE	GJ 674		1.72 ± 0.13
171	GJ 433	173.861792	-32.544918	9.077 ± 0.002	M2V	8.8967	TRUE	GJ 433		0.05 ± 0.02
177	HD 36395	82.868591	-3.689406	5.704 ± 0.001	M1.5V	7.1082	TRUE	GJ 205		0.59 ± 0.08
183	L 768-119 A	235.514844	-19.477795	9.69 ± 0.03	M3V	10.6858	FALSE	GJ 595 A		-
184	G 48-20	142.682461	0.319467	9.910 ± 0.003	M3.5V	10.5017	FALSE	GJ 1125		-
185	UPM J0815-2344 A	123.797365	-23.737305	9.897 ± 0.003	M3.5V	11.0593	TRUE			0.08 ± 0.04
186	GJ 682	264.259530	-44.324673	5.008 ± 0.001	M4V	9.6021	TRUE	GJ 682		0.10 ± 0.04
187	G 119-36 A	162.435102	35.541427	9.73 ± 0.04	M4V	11.6252	FALSE	GJ 1138 A		-
188	GJ 436	175.552054	26.701835	9.775 ± 0.003	M3V	9.5820	FALSE	GJ 436		-
191	HD 119850	206.443094	14.883051	5.435 ± 0.001	M1.5V	7.6105	TRUE	GJ 526		0.13 ± 0.03
195	YZ CMi	116.165357	3.549871	5.989 ± 0.001	M4V	9.6922	TRUE	GJ 285		9.67 ± 0.36
196	CD-44 3045 B	104.434219	-44.291824	8.041 ± 0.003	M3V	10.3819	TRUE	GJ 257 B	FLAG C	0.04 ± 0.02
197	BD-11 3759	218.567931	-12.516108	6.253 ± 0.002	M4V	9.8949	FALSE	GJ 555		-
199	G 160-28	57.681931	-6.102877	9.928 ± 0.004	M3.5V	11.4772	FALSE	GJ 1065		-
205	Ross 440 A	142.835243	-13.488438	10.0 ± 0.4	M3V	9.6544	FALSE	GJ 352 A	FLAG C	-
206	Ross 440 B	142.835386	-13.488438	10.0 ± 0.4	M2.5V	9.8487	FALSE	GJ 352 B	FLAG C	-
207	L 399-68	190.186590	-43.562373	8.052 ± 0.002	M3.5V	10.9834	TRUE	GJ 9415		0.08 ± 0.02
208	L 230-188	62.609087	-53.616320	7.108 ± 0.001	M4.5V	11.9028	TRUE	GJ 1068	Flag A	0.03 ± 0.01
210	HD 32450 B	75.617601	-21.257964	8.416 ± 0.006	M0V	9.63678	TRUE	GJ 185 B	FLAG C	0.12 ± 0.03
211	Wolf 461	195.134174	5.686880	8.545 ± 0.004	M4.5V	11.7729	TRUE	GJ 493.1		0.68 ± 0.08
217	L 205-128	266.630598	-57.326924	5.889 ± 0.002	M3V	9.5922	FALSE	GJ 693		-
223	CD-30 731	31.448775	-30.176035	9.380 ± 0.002	M3V	11.0506	TRUE	GJ 3135		0.32 ± 0.05

Table H.2: *Gaia* 10 pc FGK stars. Rate_e1 denotes the eRASS1 catalogue count rate (Merloni et al. 2024), taken from the column `ML_RATE_0_e1`, i.e., the 0.2–2.3 keV band rate. Flag A: field crowded; Flag B: optical loading; Flag C: close pair.

ID	OBJ_NAME	RA_mean	DEC_mean	D (pc)	SpT	G (mag)	eRASS1 Catlog.	Gliese Name	Comm.	Rate_e1
0	GJ 570 A	224.3731	-21.4255	5.886 ± 0.002	K4V	5.3640	TRUE	GJ 570 A	Flag A	0.98 ± 0.05
2	41 Ara Aa	259.774717	-46.635611	8.791 ± 0.006	G9V	5.3014	FALSE	GJ 666 A		0.05 ± 0.01
6	del Eri	55.811533	-9.759060	9.09 ± 0.02	K0V	3.2755	TRUE	GJ 150	Flag B	0.60 ± 0.03
9	61 UMa	175.262480	34.199415	9.576 ± 0.009	G8V	5.1109	TRUE	GJ 434		2.03 ± 0.08
10	61 Vir	199.594747	-18.317386	8.53 ± 0.01	G6.5V	4.5325	TRUE	GJ 506	Flag B	0.09 ± 0.01
12	gam Pav	321.611982	-65.361539	9.258 ± 0.009	F9V	4.0891	TRUE	GJ 827	Flag B	0.05 ± 0.01
13	eps Eri	53.226934	-9.458139	3.220 ± 0.001	K2V	3.4657	TRUE	GJ 144	Flag B	14.63 ± 0.20
15	del Pav	302.199169	-66.188646	6.099 ± 0.005	G8V	3.3641	TRUE	GJ 780	Flag B	0.41 ± 0.03
17	HD 20794	50.006059	-43.065552	6.041 ± 0.003	G6V	4.0639	TRUE	GJ 139	Flag B	0.09 ± 0.01
25	36 Oph B	258.834400	-26.609468	5.952 ± 0.005	K1V	4.8356	TRUE	GJ 663 B	Flag B C	3.31 ± 0.09
26	GJ 216 B	86.108650	-22.423890	8.892 ± 0.002	K2.5V	5.8681	TRUE	GJ 216 B		1.01 ± 0.04
28	HD 50281 A	103.072033	-5.173733	8.745 ± 0.003	K3.5V	6.2310	TRUE	GJ 250 A		0.74 ± 0.05
32	36 Oph A	258.834400	-26.609468	5.948 ± 0.004	K2V	4.8285	TRUE	GJ 663 A	Flag B C	3.31 ± 0.09
34	pi.03 Ori	72.462767	6.961347	8.02 ± 0.01	F6V	3.0879	TRUE	GJ 178	Flag B	12.63 ± 0.17
35	eps Ind A	330.882374	-56.800743	3.638 ± 0.001	K5	4.3229	TRUE	GJ 845 A	Flag B	1.36 ± 0.06
36	GJ 66 A	24.951421	-56.196385	8.196 ± 0.002	K2V	5.6254	TRUE	GJ 66 A	GJ 66 B C	0.52 ± 0.03
38	bet Hyi	6.496340	-77.252346	7.48 ± 0.02	G0V	2.6807	TRUE	GJ 19	Flag B	2.95 ± 0.07
39	HD 102365 A	176.617751	-40.498010	9.319 ± 0.008	G2V	4.7016	TRUE	GJ 442 A	Flag B	0.04 ± 0.01
41	GJ 216 A	86.113957	-22.450530	8.91 ± 0.01	F6V	3.4768	TRUE	GJ 216 A	Flag B	0.34 ± 0.02
43	GJ 166 A	63.804843	-7.672785	5.010 ± 0.003	K0V	4.1798	TRUE	GJ 166 A	Flag A B	0.47 ± 0.03
44	HD 100623 A	173.618218	-32.826553	9.559 ± 0.003	K0V	5.7383	TRUE	GJ 432 A		0.06 ± 0.01
45	36 Oph C	259.052557	-26.552693	5.954 ± 0.001	K5V	5.8898	TRUE	GJ 664		0.84 ± 0.04
46	HD 32147	75.207377	-5.760124	8.844 ± 0.002	K3	5.8864	TRUE	GJ 183		0.13 ± 0.02
49	GJ 66 B	24.951421	-56.196385	8.189 ± 0.002	K2V	5.5083	TRUE	GJ 66 B	Flag C	0.52 ± 0.03
50	chi01 Ori A	88.594562	20.275727	8.70 ± 0.04	G0V	4.2416	FALSE	GJ 222	Flag B	-
52	ksi UMa Ba	169.542832	31.525579	8.73 ± 0.03	G2V	4.6402	TRUE	GJ 423 Ba	Flag B	29.07 ± 0.31
53	zet Tuc	5.041138	-64.868014	8.61 ± 0.01	F9.5V	4.0735	TRUE	GJ 17	Flag B	0.09 ± 0.01

Continued on next page

ID	OBJ_NAME	RA_mean	DEC_mean	D (pc)	SpT	G (mag)	eRASS1 Catlog.	Gliese Name	Comm.	Rate_e1
57	Alpha Centauri A	219.85820	-60.831234	1.34	G2V	–	TRUE	GJ 559 A	Flag B C	14.93 ± 1.64
58	Procyon A	114.821329	5.218964	3.50	F5V	–	TRUE	GJ 280	Flag B	8.20 ± 0.21
59	Alpha Centauri B	219.85820	-60.831228	1.34	K1V	–	TRUE	GJ 559 B	Flag B C	14.93 ± 1.64
60	HD 156384 A	259.746199	-34.990209	6.80	K3V	–	TRUE	GJ 667 A	Flag B C	0.80 ± 0.04
61	HD 156384 B	259.746199	-34.990209	6.80	K5V	–	FALSE	GJ 667 B	Flag B C	-